CHALMERS
UNIVERSITY OF TECHNOLOGY

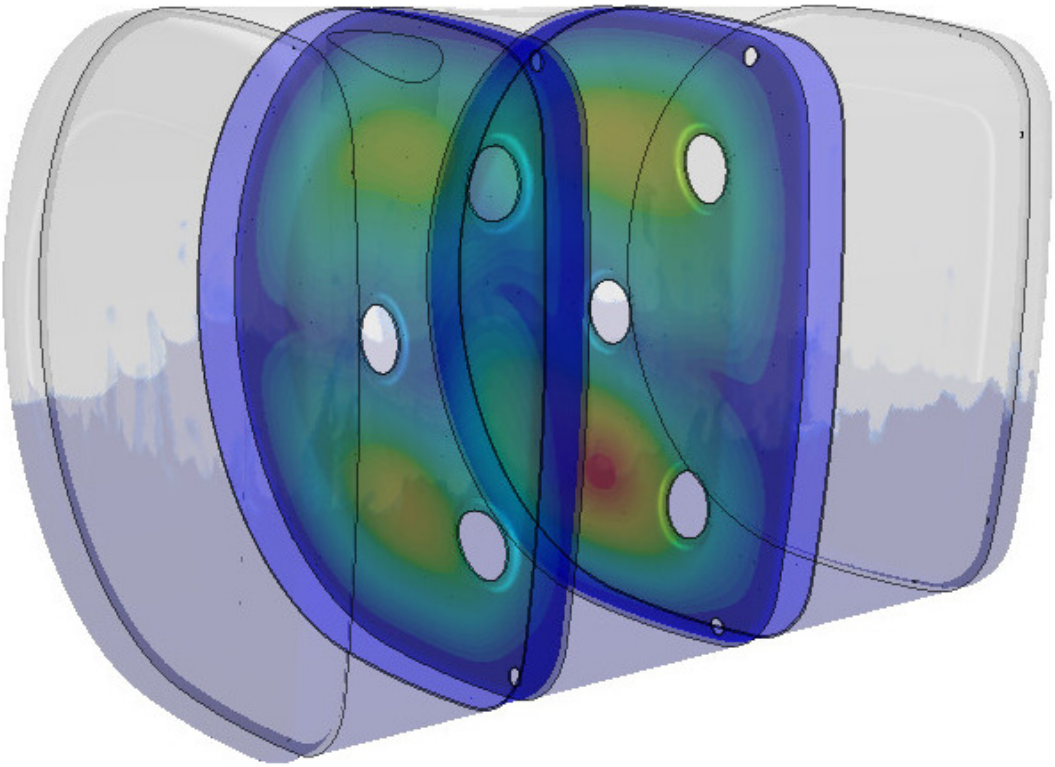

Analysis of sloshing-induced loads on the fuel tank structure

Master's thesis in Applied Mechanics

Sampann Arora
Sudharsan Vasudevan

Department of Mechanics and Maritime Sciences
CHALMERS UNIVERSITY OF TECHNOLOGY
Gothenburg, Sweden 2017

Master's thesis 2017:77

Analysis of sloshing-induced loads on the fuel tank structure

A coupled CFD-FEA methodology to analyse sloshing-induced loads

SAMPANN ARORA
SUDHARSAN VASUDEVAN

CHALMERS
UNIVERSITY OF TECHNOLOGY

Department of Mechanics and Maritime Sciences
Division of Fluid Dynamics
Chalmers University of Technology
Gothenburg, Sweden 2017

Analysis of sloshing-induced loads on the fuel tank structure
SAMPANN ARORA
SUDHARSAN VASUDEVAN

Master's Thesis 2017:77
Department of Mechanics and Maritime Sciences
Division of Fluid Dynamics
Chalmers University of Technology
SE-412 96 Gothenburg
Telephone +46 31 772 1000

Supervisor:	Sassan Etemad, Volvo Group Trucks Technology and Chalmers University of Technology
Supervisor:	Srdjan Sasic, Chalmers University of Technology
Examiner:	Sassan Etemad, Volvo Group Trucks Technology and Chalmers University of Technology

Cover: Volvo D-shaped fuel tank showing the fluid domain coloured by volume fraction of water and contours of displacement on the baffles

Typeset in LaTeX
Gothenburg, Sweden 2017

Analysis of sloshing-induced loads on the fuel tank structure
SAMPANN ARORA
SUDHARSAN VASUDEVAN
Department of Mechanics and Maritime Sciences
Division of Fluid Dynamics
Chalmers University of Technology

Abstract

Fuel sloshing is a source of major concern in the structural design of fuel tanks in heavy duty trucks. It is caused due to the free surface motion of fuel in partially filled containers induced by external agitation. With capacities as high as 900 litres, this phenomenon is capable of causing fuel to impact the container tank with high forces, exposing the vulnerable parts of the tank to heavy dynamic loads. This highly non-linear phenomenon is simulated using the commercial computational fluid dynamics (CFD) code STAR-CCM+. The two phase (air-fuel) problem is solved using the volume of fluid (VOF) interface capturing approach. Owing to the thin walled structures of the fuel tank, it becomes indispensable to cater to the effects of fluid-structure interaction (FSI). This need is amplified with the ever-increasing design constraints and use of novel materials for fuel tanks aiming at weight reduction. To this end, a partitioned FSI methodology is employed by coupling the CFD and Finite Element Analysis (FEA) solvers for this multi-physics problem. The results of one-way and two-way coupled FSI analyses are compared with experiments and a sufficient level of accuracy is obtained. This coupling strategy could inform a fuel tank design suited to prevent structural damage due to sloshing, contributing towards the safety and longevity of the fuel tank.

Keywords: Fuel Tanks, Sloshing, Volume of Fluid, Partitioned Fluid Structure Interaction.

Acknowledgements

This thesis is an outcome of the immense support and motivation from our supervisor, Prof. Sassan Etemad. Sassan, we thank you for sharing meaningful insights and for guiding us in times of standstill — technical and administrative alike. We also thank our co-supervisor, Prof. Srdjan Sasic, for kindling our curiosity and for providing us with invaluable guidance in the field of multiphase flow modelling. We appreciate the guidance on the structural side by Mikael Boisen. Regular brainstorming sessions at Volvo with Sigurd Sonderegger, Mikael Boisen and Sondre Landvik gave us vital information on the broader objective of this project and propelled us towards thinking in the right direction. We also thank Sassan and Mikael for providing us with the surface meshes of the full-scale tank model. Thank you Torbjörn Wiklund and Sebastien Ragot for clarifying our STAR-CCM+ and Abaqus related questions, respectively. We are grateful to Dennis Engberg for arranging access to the software and cluster at Volvo, and his continuous support throughout the project. Many thanks to the amazing support team at CD-adapco's London office. A special mention to Hjalmar Sandberg for always welcoming the discussions related to experimental testing. We extend our gratitude to our group managers Peter Nilsson and Jonas Andersson for their constant encouragement and for providing us with the most comfortable working environment. Special thanks to Peter Nilsson for going out of his way toward extending our tenure at Volvo that provided us with the essential time for the completion of this project. Lastly, we would like to commend ourselves for putting up with each other's idiosyncrasies in the best interest of this thesis.

Sampann Arora, Sudharsan Vasudevan, Gothenburg, August, 2017

Nomenclature

Abbreviation

API	Application Program Interface
CFD	Computational Fluid Dynamics
CSE	Co-Simulation Engine
FEA	Finite Element Analysis
FSI	Fluid Structure Interaction
HRIC	High Resolution Interface Capturing
RMS	Root Mean Squared
UD	Upwind Differeincing
VOF	Volume of Fluid

Symbols

α	Volume fraction
δ, γ	Constants in Newmark method
ϵ	Turbulent dissipation
Γ_s	Fluid-solid interface
λ, G	Lame's constants
$\mathbf{C}$	Damping matrix
$\mathbf{f_{ext}}$	Externally applied loads
$\mathbf{f_{int}}$	Internal forces
$\mathbf{K}$	Stiffness matrix
$\mathbf{M}$	Mass matrix
$\mathbf{u}$	Solid displacement vector
μ	Dynamic viscosity
μ_t	Turbulent viscosity
ν	Poisson's ratio

Ω	Vorticity tensor
ω	Angular velocity
$\overline{v_i}$	Time averaged velocity
ρ	Density
σ	Stress tensor
τ	Shear stress tensor
C_α	Sharpening factor in surface compression term
c_μ,C_{1e},C_2,σ_k,σ_ϵ	Model constants in Realizable $k-\epsilon$ turbulence model
Cu	Courant Number
Cu_l	Lower Courant Number
Cu_u	Upper Courant Number
E	Young's Modulus
f	Body force
k	Turbulent kinetic energy
p	Pressure
P_b	Production term for turbulent kinetic energy due to buoyancy
P_k	Production term for turbulent kinetic energy due to mean velocity gradients
S	Strain rate tensor
S_ϵ	Source term in transport equation for turbulent dissipation
S_k	Source term in transport equation for turbulent kinetic energy
s_α	Source term in transport equation for phase indicator function
t	Time
u_r	Velocity at the liquid-air interface
V	Volume
v	Instantaneous velocity
v''	Fluctuating velocity
v^g	Grid velocity
v_r	Modelled relative velocity in the surface compression term
Y_M	Contribution of fluctuating dilatation in compressible turbulence to the overall dissipation rate

Contents

List of Figures

1
Introduction

Analysis of liquid sloshing poses an interesting challenge in computational mechanics due to the complex underlying physics. Simulation of such problems involves an accurate modelling of the two-phase flow problem as well as accounting for the sloshing impacts on the solid structure through coupled fluid-solid interactions [1]. Such simulations have found their place in a variety of industrial applications, for instance, in the directional stability of liquid tank vehicles [2], pressure vessels of nuclear reactors built to withstand loads due to seismic excitation [3, 4], and fuel tanks in the aerospace and automotive industries [5, 6]. Experimental investigation of sloshing effects is often labour-intensive and costly. Moreover, the locations of gauges and sensors in an experimental rig require a prior knowledge of vulnerable areas of the tank structure. Simulations can help obtain critical information on the structure and design of fuel tanks at an early phase, thus significantly reducing the lead times in the manufacturing process. Also, the advent of novel materials like plastics and composites, aimed at over-all weight reduction, has made such an analysis procedure an absolute necessity.

Several studies analyze the effects of the dynamic sloshing impacts on the fuel tank structure. Investigations show that sloshing loads depend on the frequency of the excitation signals and these loads become maximum when the excitation frequency is close to the natural frequency of the liquid in the tank [7, 8]. Numerical models have also been used to predict sloshing induced noise in fuel tanks by analyzing the surface impact pressures [9, 10]. The effect of baffles in reducing sloshing motion has been explored extensively in rectangular tank geometries through experimental and numerical investigations [11–14]. Simulations on prismatic tanks with elastic baffles have also been studied using coupled fluid-solid interaction methodologies [15, 16]. These representative test cases on simplified geometries provide validation data for model formulations using different numerical and analytical techniques.

Fuel tanks of heavy duty Volvo trucks are usually made of Aluminium. The D-shaped body, reinforced with baffles, constitutes the tank structure (Figure 1.1). The baffles provide structural rigidity and dampen the effect of strong sloshing waves. However, during test runs, cracks and leakages have been observed due to the sloshing impacts leading to eventual failure of the tank structure (Figure 1.2). The existing structural analysis methodology at Volvo does not account for the effects of sloshing and therefore, has to rely on experimental investigations. This calls for the need of a comprehensive numerical model to accurately predict the effect of sloshing on the fuel tank structure.

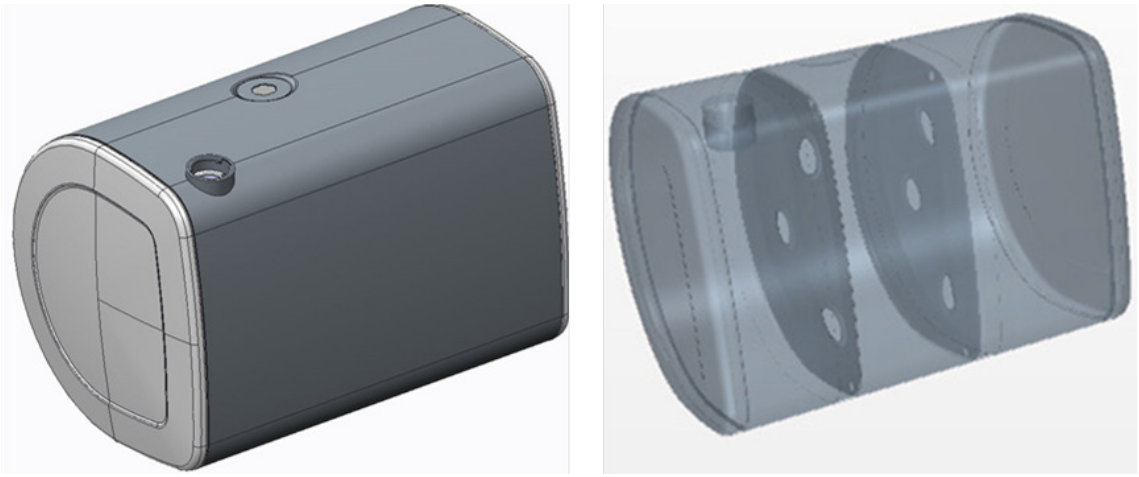

Figure 1.1: Fuel tank for heavy duty Volvo trucks

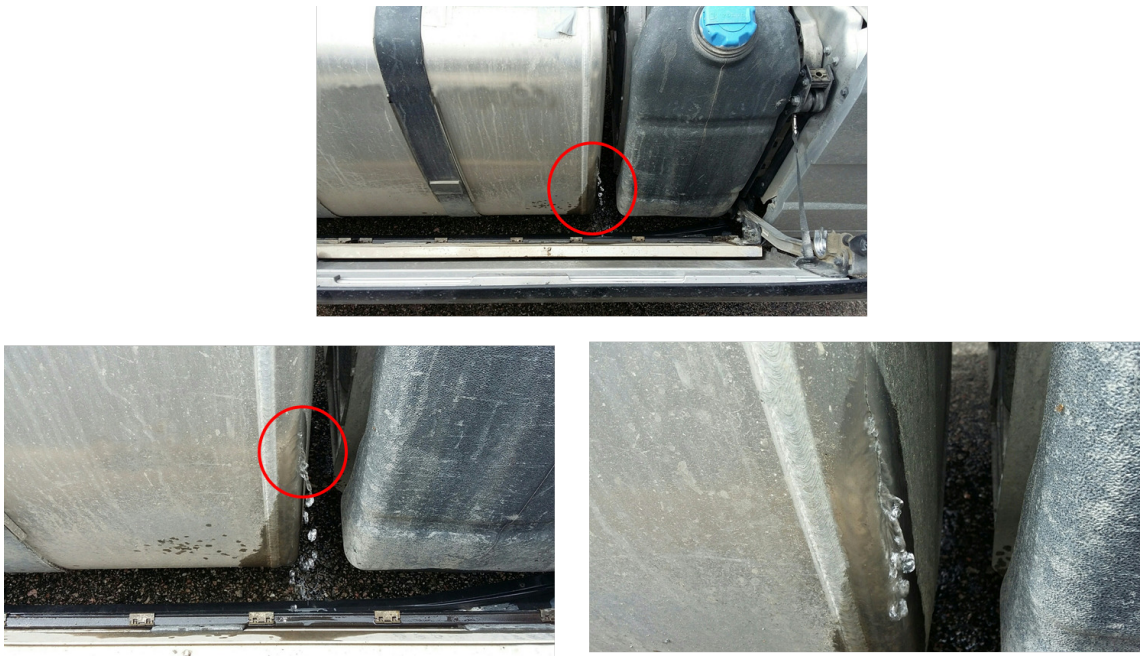

Figure 1.2: Cracks observed on the end plates of an excessively loaded tank

This thesis aims at presenting a partitioned fluid structure interaction (FSI) methodology for the analysis of fuel sloshing-induced stresses on the walls and baffles of a fuel tank. A computational fluid dynamics (CFD) methodology using the volume of fluid (VOF) model, validated against existing numerical and experimental results in the literature for a simplified geometry, is first presented. This is then extended by adding flexible components in the solid domain, which is solved using finite element analysis (FEA). The coupled CFD-FEA methodology for these validated benchmark cases lays the foundation for the three dimensional FSI analysis of a representative fuel tank model and thereafter, the complete fuel tank of a heavy duty Volvo truck.

The FSI coupling module in STAR-CCM+ with an in-built finite-element structural solver is used in the present study. Results from *one-way* and *two-way*[1] coupled FSI strategies are compared with experiments conducted at Volvo. The possibilities of coupling STAR-CCM+ with an external FEA code 'Abaqus' using Simulia's Co-Simulation Engine (CSE) are also explored. The ultimate aim of this work is to provide an accurate and computationally economical numerical model. This generic methodology can be adopted for analyzing other sloshing prone components in the truck, for instance, the Adblue tank and large liquid containing trailers.

1.1 Thesis Outline

The thesis is divided into five chapters. The motivation and broad contents of the study are outlined in this chapter. The theoretical background of the numerical models and the coupling strategies are covered in the chapter 2. Chapter 3 includes the methods of model implementation along with the validation studies. The results from validation studies are also included in chapter 3 since these corroborate the model parameters for the numerical setup of the full-scale tank geometry. Results and discussions of the coupled CFD-FEA studies on a representative tank and the Volvo fuel tank are covered in chapter 4. Finally, conclusions as well as discussions on the scope for future investigations are included in chapter 5. Some additional information and results are included in the Appendix.

1.2 Assumptions and Limitations

Apart from the validation studies, FSI simulations are performed only on one tank geometry since the experimental data for only one fuel-tank model was available. For safety reasons, experimental investigations in the test rig are performed using water. Therefore, simulations are also performed using water as the liquid phase. Effects of inter-phase mass transfer, surface tension and compressibility effects have not been in the CFD model. The analysis is only specific to the fuel tank structure and therefore, the vibrational effects of the surrounding structural members are not considered.

[1] see subsection 2.2.2 for a background on one-way and two-way coupled FSI strategies

2
Theory

In this section the theoretical background of the volume of fluid (VOF) and the partitioned fluid-structure interaction (FSI) methods is discussed in detail. The equations are presented in the standard tensor (or index) notation.

2.1 Modelling Two-Phase Flows

Multiphase flows are characterized by the simultaneous presence of multiple interacting phases, such as gas-solid, gas-liquid and liquid-liquid, in a domain of interest. Depending on the range of spatial and temporal scales, different modelling techniques exist. Modelling of multiphase flows is broadly classified into Eulerian–Lagrangian (EL) and Eulerian–Eulerian (EE) methods. The EL method is typically used to model interactions at the particle level, for instance, in spray modelling, particle-laden flows, contact and collision dominated flow systems, etc. The dispersed phase is solved in a Lagrangian framework, using the Newton's laws of motion and the continuous phase is solved in an Eulerian framework. The EE method, on the other hand, treats all the phases in the system in a continuum description, with model terms for interphase mass, momentum and energy exchange in the governing equations. This method is generally employed when interest is in the continuous flow properties rather than at the particle level.

The phenomenon of sloshing falls under the category of multiphase flows, characterized by the free surface motion at the interface of a liquid-air system. Due to the non-linear motion and severe topological changes of the free surface, it is important to efficiently resolve the interface of the two fluids. There exist several mathematical models in the literature to numerically simulate the sloshing phenomenon by accurate prediction of the interface. These models can be classified into particle-based and grid-based methods. A commonly used particle based method for free surface flows in liquid sloshing applications is the Smoothed Particle Hydrodynamics (SPH) method, wherein the fluid domain comprises of a set of particles tracked using the Lagrangian approach [17, 18]. Interface diffusion is not an issue since it is tracked by particle locations and violent waves can therefore be simulated accurately. However, for complex three-dimensional geometries, such simulations become computationally expensive [19]. Also, complicated boundary treatments and limited applications put further constraints on the usage of SPH in industrial research and development [20, 21].

Among grid-based methods, the most widely used are the VOF and level-set methods. These methods are based on the continuum-description, with a single set of governing equations for the fluid phases and additional equations accounting for advection of the interface. Level-set is based on a distance function formulation to track the interface, wherein the vanishing magnitude of the distance function gives the location of the interface [24]. Although it is known to accurately capture the interface, the level-set method is not mass-conservative. The VOF method uses the color function to implicitly capture the interface [25]. It is efficient in ensuring mass conservation but it also has disadvantages in that it is not able to accurately capture the surface curvature and spatial derivatives due to the sharp discontinuity near the interface. There have been several studies involving coupling of the level-set and VOF methods to overcome the disadvantages of each method [26, 27]. This approach, however, is out of scope of the present study but can be implemented in a future work.

In this study, the VOF method provided in the commercial code STAR-CCM+ is used for the two-phase flow problem. Given its effectiveness in handling free surface flows for complex three-dimensional geometries using unstructured meshes, it has been widely exploited in industry and academia alike for sloshing based problems [14, 29–31]. The mathematical formulation and underlying schemes of the VOF method are discussed in the next section.

2.1.1 Volume of Fluid Method

Numerical simulation of an incompressible fluid flow problem is performed by solving three equations - continuity (mass conservation), Navier-Stokes (momentum conservation) and energy conservation. When the effects of heat transfer are not significant, the energy conservation equation is neglected and therefore will not be discussed here.
The continuity equation is given by

$$\frac{\partial v_i}{\partial x_i} = 0 \tag{2.1}$$

The Navier-Stokes equation is given by

$$\rho\frac{\partial(v_i)}{\partial t} + \rho\frac{\partial(v_i v_j)}{\partial x_j} = -\frac{\partial p}{\partial x_i} + \mu\frac{\partial^2 v_i}{\partial x_j \partial x_j} + \rho g_i \tag{2.2}$$

The aforementioned governing equations are applicable for a single phase fluid flow problem. In case of fuel sloshing, two phases (fuel and air) are involved. Hence, additional models are required to simulate this multiphase flow phenomenon.

The VOF model is used in analysing immiscible fluids with distinctly defined interface. This model implicitly captures the interface and hence is very efficient in modelling flow problems where the shape of the interface is of interest. The fractional amount of fluid (volume fraction) in a particular cell, that acts as a phase

indicator function, is employed. The volume fraction of the ith phase in a cell within a multiphase domain is given by

$$\alpha_i = \frac{V_i}{V} \tag{2.3}$$

Where, V_i is the volume of the ith phase in the cell and V is the volume of the cell. In a domain with two phases, the phase indicator function is defined as

- $\alpha_1 = 1$ if the cell is filled with phase-1
- $\alpha_1 = 0$ if the cell is filled with phase-2
- $0 < \alpha_1 < 1$ if the cell contains the interface

In the VOF model, the domain is modelled as a single fluid, whose density and viscosity are defined using the phase indicator function.

$$\rho = \alpha_i \rho_i \tag{2.4}$$

$$\mu = \alpha_i \mu_i \tag{2.5}$$

The above mentioned equivalent density and viscosity are used in the governing equations, Equation 2.1 and Equation 2.2, to solve the two-phase flow problem.

In addition to these, the evolution of the interface with space and time is governed by the transport equation of the phase indicator function

$$\frac{\partial \alpha_1}{\partial t} + \frac{\partial (\alpha_1 v_i)}{\partial x_i} + \frac{\partial (v_{r,i} \alpha_1 (1 - \alpha_1))}{\partial x_i} = s_{\alpha_1} \tag{2.6}$$

The first two terms on the left hand side of Equation 2.6 are the unsteady and convection terms, respectively. The third term on the left hand side is known as the surface compression term and it contributes only in the interface ($0 < \alpha_1 < 1$) [23]. This term mitigates the effect of numerical diffusion and results in a sharp interface. In this term, $v_{r,i}$ is the relative velocity between the two phases and it is approximated based on the fluid velocity at the interface. In STAR-CCM+, the relative velocity in the surface compression term is modelled as

$$v_{r,i} = C_\alpha |u_{r,i}| \frac{\nabla \alpha_1}{|\nabla \alpha_1|} \tag{2.7}$$

Where, $u_{r,i}$ is the velocity at the interface and C_α is known as the sharpening factor. The sharpening factor accepts values in the interval [0,1]. The right hand side of Equation 2.6 is the source or sink term for phase-1. Since, the effects of phase change and reduction in fuel quantity due to consumption are not considered, this term is insignificant for the current study. A similar transport equation can be written for the other phase in the domain.

The transport equation for the phase indicator function determines the fractional volume of the fluids in the domain cells, which is reflected in the Navier-stokes equation through the equivalent density and viscosity (Equations 2.4, 2.5). The velocity obtained from the Navier-Stokes and continuity equations is reflected in the convective term of transport equation for phase indicator function. Thus, the three governing equations (Equation 2.1, Equation 2.2 and Equation 2.6) are solved

together to capture the interface implicitly.

It is to be noted that STAR-CCM+ restricts the solver to a segregated flow solver when the VOF model is chosen. Therefore, the SIMPLE algorithm, in combination with a collocated variable arrangement and Rhie-Chow interpolation, are used to solve the pressure-velocity coupling.

The discretization scheme used for the convection term in the transport equation of the phase indicator function has a direct impact on the sharpness of the interface. Lower order schemes, despite being numerically stable, are diffusive in nature and hence result in a smeared interface. Higher order schemes on the other hand are less diffusive but unstable. The scheme used in this work is a blend of the second order accurate High Resolution Interface Capturing (HRIC) scheme and the first order accurate Upwind Differencing (UD) scheme. The two schemes are implemented based on the local Courant number of the control volume as

- HRIC, when $Cu < Cu_l$
- Blend of HRIC and UD, when $Cu_l \leq Cu \leq Cu_u$
- UD, when $Cu > Cu_u$

Where, Cu is the local Courant number; Cu_l and Cu_u are the lower and upper limits set as 0.5 and 1, respectively. The controlled blending brings both accuracy and stability in this numerical scheme.

The continuity (Equation 2.1) and Navier-Stokes (Equation 2.2) equations are time averaged to obtain the Unsteady Reynolds Averaged Navier Stokes (URANS) equations, given as

$$\frac{\partial \overline{v_i}}{\partial x_i} = 0 \tag{2.8}$$

$$\frac{\partial \overline{v_i}}{\partial t} + \frac{\partial (\overline{v_i}\ \overline{v_i})}{\partial x_j} = -\frac{1}{\rho}\frac{\partial \overline{p}}{\partial x_i} + \frac{\mu}{\rho}\frac{\partial^2 \overline{v_i}}{\partial x_j \partial x_j} - \frac{\partial \overline{v''_i v''_j}}{\partial x_j} \tag{2.9}$$

where $\overline{v_i}$ is the time averaged velocity and v''_i is the fluctuating velocity.

The last term on the right hand side of Equation 2.9 is the Reynolds stress tensor and a turbulence model is required to model this term. Although Large Eddy Simulations (LES) give accurate results, they are computationally very expensive. Therefore, a two equation eddy viscosity model called the *realizable* $k-\epsilon$ model is used, where, k is the turbulent kinetic energy and ϵ is turbulent dissipation. This model has been widely used in analyzing sloshing flows, yielding fairly accurate results [28, 29]. The transport equations of the turbulent kinetic energy and turbulent dissipation rate are given as

$$\frac{\partial}{\partial t}(\rho k) + \frac{\partial}{\partial x_j}(\rho k v_j) = \frac{\partial}{\partial x_j}[(\mu + \frac{\mu_t}{\sigma_k})\frac{\partial k}{\partial x_j}] + P_k + P_b - \rho\epsilon - Y_M + S_k \tag{2.10}$$

$$\frac{\partial}{\partial t}(\rho\epsilon) + \frac{\partial}{\partial x_j}(\rho\epsilon v_j) = \frac{\partial}{\partial x_j}[(\mu + \frac{\mu_t}{\sigma_\epsilon})\frac{\partial \epsilon}{\partial x_j}] + \rho C_1 S\epsilon - \rho C_2 \frac{\epsilon^2}{k + \sqrt{\nu\epsilon}} + C_{1\epsilon}\frac{\epsilon}{k}C_{3\epsilon}P_b + S_\epsilon \tag{2.11}$$

Where,

$$C_1 = max[0.43, \frac{\eta}{\eta + 5}], \eta = S\frac{k}{\epsilon}, S = \sqrt{2S_{ij}S_{ij}}$$

In the above equations, P_k is the production term for turbulent kinetic energy due to mean velocity gradients and P_b is the production term for turbulent kinetic energy due to buoyancy. Y_M represents the contribution of the fluctuating dilatation in compressible turbulence to the overall dissipation rate. The turbulent viscosity μ_t is modelled as

$$\mu_t = \rho c_\mu \frac{k^2}{\epsilon} \tag{2.12}$$

It is to be noted that, the transport equation for turbulent dissipation in the Realizable $k - \epsilon$ model is different from the standard $k - \epsilon$ model. Also, unlike the standard $k - \epsilon$ model, c_μ is defined as a function of the mean flow and turbulence properties.

$$c_\mu = \frac{1}{A_0 + A_s\frac{kU^*}{\epsilon}}$$

where

$$U^* = \sqrt{S_{ij}S_{ij} + \tilde{\Omega_{ij}}\tilde{\Omega_{ij}}}$$
$$\tilde{\Omega_{ij}} = \Omega_{ij} - 2\epsilon_{ijk}\omega_k$$
$$\Omega_{ij} = \overline{\Omega_{ij}} - \epsilon_{ijk}\omega_k$$
$$A_0 = 4.06, A_s = \sqrt{6}cos\phi$$
$$\phi = \frac{1}{3}cos^{-1}(\sqrt{6}W), W = \frac{S_{ij}S_{jk}S_{ki}}{\tilde{S}^3}, \tilde{S} = \sqrt{S_{ij}S_{ij}}, S_{ij} = \frac{1}{2}(\frac{\partial v_j}{\partial x_i} + \frac{\partial v_i}{\partial x_j})$$

The term $\overline{\Omega_{ij}}$ is the mean rate-of-rotation tensor viewed in a rotating reference frame with the angular velocity ω_k. Further, the model constants for this turbulence model are given by,

$$C_{1\epsilon} = 1.44, C_2 = 1.9, \sigma_k = 1.0, \sigma_\epsilon = 1.2$$

This turbulence model ensures satisfaction of two reliability criteria viz., positivity of normal Reynolds stresses and Schwarz inequality of turbulent shear stress [32]. In addition to this, implementation of 'two layer approach', provides the advantage of modelling the near-wall turbulence for any first layer cell height (all y+ wall treatment) [33].

2.2 Fluid-Structure Interaction

The scope of physics involving FSI is wide and far-reaching. It is observed in aerodynamic flutter, cardiovascular system, particle-laden flows, engines and heat exchangers, free surface flows, and so forth. These examples are characterized by the simultaneous presence of fluid and solid domains, interacting at a wide range of spatial and temporal scales. The effects of FSI problems become relevant when these scales are significant in influencing the physics of each domain interdependently, thus requiring a *coupled* framework to solve the governing equations pertaining to both domains.

Problems involving fluid structure interactions can be solved through a *monolithic* or a *partitioned* approach. Governing equations for the fluid and structure domains are solved simultaneously in the monolithic approach within one system of equations [34, 35]. Such an approach results in a robust and numerically accurate method, ensuring convergence between solid and fluid domains, but at very high computational costs [36]. Algorithms and codes using this approach generally have to be tailor-made to suit a particular problem, rendering its re-usability and versatility limited.

In the partitioned approach, the fluid and solid domains are solved for separately in their respective solvers, and the exchange of field variables across the domains takes place through an interface. Thus, the coupled problem can be solved by means of separate grids, dedicated solvers and algorithms for each domain. This makes the partitioned approach more flexible than the monolithic approach. However, this comes at an added expense that the interface conditions need to be carefully handled, especially in cases of large structural deformations [37]. The different discretization schemes for the fluid and solid solvers also require a consistent transfer of field variables across the domains. Efficient data mapping at the solid-fluid interface and mesh morphing techniques are therefore necessary to solve FSI problems using the partitioned approach [38, 39]. For the aforementioned reasons of solver independence and the flexibility to use non-conformal unstructured grids for fluid and solid domains, the partitioned approach is explored in the present study using the FSI module within STAR-CCM+, and also using an external Application Program Interface (API) for coupling STAR-CCM+ and Abaqus codes.

2.2.1 Governing Equations

The general conservation equation of linear momentum, valid for both fluid and solid domains, is given by

$$\rho \dot{v}_i - \sigma_{ij,j} + f_i = 0 \tag{2.13}$$

The second term in Equation 2.13 is the stress term and is expressed differently for the fluid and solid domains. For a Newtonian incompressible fluid, this term is expressed in terms of the pressure and shear stresses as given below

$$\sigma^f_{ij,j} = -p\delta_{ij} + \tau_{ij} \tag{2.14}$$

where superscript f denotes the fluid domain.

Using this constitutive relationship, the Navier-Stokes equations (Equation 2.2) can be derived.

The inertial stress term for a linear elastic isotropic solid is given by the Hooke's law. The stress and strain are linearly related and the constitutive is relation given by

$$\sigma_{ij}^{s} = \lambda \delta_{ij} \epsilon_{kk} + 2G\epsilon_{ij} \tag{2.15}$$

where superscript s denotes the solid domain.

The strain ϵ_{ij} and the Lame's constants (λ and G) are defined as

$$\epsilon_{ij} = \frac{1}{2}(u_{i,j} + u_{j,i}) \tag{2.16}$$

$$G = \frac{E}{2(1+\nu)} \tag{2.17}$$

$$\lambda = \frac{E\nu}{(1+\nu)(1-2\nu)} \tag{2.18}$$

Where E is the Young's modulus, ν is the Poisson's ratio and u_i are the displacements.

In FE formulation, the governing equation for the solid domain is given by

$$\mathbf{M\ddot{u} + C\dot{u} = f_{ext} - f_{int}} \tag{2.19}$$

where $\mathbf{M}$ is the mass matrix and $\mathbf{C}$ is the damping matrix. f_{ext} denotes the externally applied loads and the stiffness matrix $\mathbf{K}$ is related to the internal force f_{int} through the displacement term as

$$\mathbf{K} = \frac{\partial \mathbf{f_{int}}}{\partial \mathbf{u}} \tag{2.20}$$

A second order accurate Newmark method is used for expressing velocity and acceleration in terms of displacement, which is in turn sought for as the solution of this dynamic problem. The velocity and displacement at time step n are given by

$$\mathbf{\dot{u}^n = \dot{u}^{n-1} + (\delta \ddot{u}^n + (1-\delta)\ddot{u}^{n-1})\Delta t} \tag{2.21}$$

$$\mathbf{u^n = u^{n-1} + \dot{u}^{n-1}\Delta t + (\gamma \ddot{u}^n + (\frac{1}{2} - \gamma)\ddot{u}^{n-1})\Delta t^2} \tag{2.22}$$

where δ and γ take values 0.5 and 0.25, respectively.

In addition to the governing equations, Dirichlet and Neumann boundary conditions are specified at the fluid-solid interface Γ_s to maintain the no-slip condition

$$v_i^s = v_i^f \quad on \quad \Gamma_s, \tag{2.23}$$

$$\sigma_{ij}^s n_i = \sigma_{ij}^f n_i \quad on \quad \Gamma_s, \tag{2.24}$$

The Neumann condition in Equation 2.24 can also also be interpreted as a displacement condition at the interface, which is considered as a Dirichlet condition in some FSI methods [39]

$$x_i^s = x_i^f, \quad on \quad \Gamma_s \tag{2.25}$$

2.2.2 The Fluid-Solid Interface and Mesh Morphing

In the partitioned approach, the fluid and solid domains are meshed with different topologies. This necessitates an efficient method of field variables exchange at the interface, as mentioned above. Data mapping with interpolation schemes that are accurate, continuous, bounded and conservative are preferred. Since FSI simulations involve mesh movement, data mappers perform a neighbour search to match the neighbours of faces on one side of the interface to the faces on the other at a reference configuration [33]. The reference configuration can either be the original mesh or the current mesh. However, having the original mesh as the reference configuration is preferred to stay computationally economical. This assumes that the faces that were neighbours in the reference configuration stay as neighbours throughout.

The pressure and wall shear stress from fluid side of the interface are mapped as forces and moments at the solid side of the interface, that act as the loads to the deformable solid domain. The displacement is mapped from the solid side to the fluid side, altering the flow field by modifying its volume mesh. This modification is performed by a mesh morpher in STAR-CCM+ by first collecting the known displacements at the boundary (fluid-solid interface) nodes, also referred to as control points. An interpolation field is then computed for the fluid region based on the displacement of these control points. The mesh vertices are displaced according to the obtained interpolation filed, thus morphing the fluid mesh [33]. The number of control points involved in computing the interpolation field in the morphing process can be adjusted by using the morpher thin-out factor.

Since the solid domain is solved in the Lagrangian formulation and the fluid domain in the Eulerian, an efficient way of accounting for the effect of the solid displacement on the fluid domain is required. This is done by using grid velocities in the fluid transport equations arising from the solid displacements through a technique known as the Arbitrary Eulerian Lagrangian (ALE) formulation. For the flow equations and their derivation based on the ALE formulation, see [40, 41].

The above description pertains to a *two-way coupled* FSI methodology, wherein the effects of both the domains are accounted for. In the present study, this is done by making the fluid and solid solvers communicate with each other for several sub-iterations within a fluid time-step. The pressure and wall shear stress from the

fluid solver are mapped on the solid domain as loads, the solid solver then gives displacements at the FSI interface and finally, the fluid mesh is morphed — this cycle repeats every inner iteration. In the *one-way coupled* FSI methodology, the fluid field variables are supplied as boundary loads on the solid domain but the effect of the resultant displacements from the solid solver on fluid domain is disregarded. Thus, there is no mesh morphing involved in this methodology. This holds correct when the solid deformations are too small to affect any changes in the flow field, for example, in cases of high solid stiffness and large solid-fluid density ratios. In the present study, both one-way and two-way coupled FSI methodologies are explored and differences in context of liquid sloshing applications are compared.

3
Methods

The model parameters used in a numerical setup for solving problems in continuum mechanics are deemed accurate if they can reproduce and replicate the experimental results within acceptable limits. However, issues like complex geometries, expensive apparatus, need for extreme precision, and so forth render such experimental data scarce. It becomes important, therefore, to validate results using a benchmark case with simplified geometry and boundary conditions so that the main problem can follow suit. Such a study is important for the present work since an accurate numerical setup for the Volvo fuel tank depends on validated studies for the physics concerning the fluid as well as the solid domain.

In the following sections, validation studies for the VOF method, i.e., the CFD only part, and the coupled CFD-FEA method are presented. A comparative analysis of coupling two separate CFD and FEA solvers with the FSI module within STAR-CCM+ is also made. Finally, the simulation methodologies for the Volvo fuel tank and a simplified representative tank are discussed.

3.1 Validation and Preliminary Studies

3.1.1 Volume of Fluid Method

Although interface capturing is the essence of using the VOF method for liquid sloshing applications, visual inspection of an accurately captured interface can be insufficient for a definitive assessment of the model, wherein the impact of sloshing on the tank structure is critical. Therefore, pressure signals — as an outcome of an accurately captured (water-air) interface — were chosen for a quantitative comparison in the validation study.

The experimental and numerical results on a simplified tank geometry are chosen for this validation based on one of the test cases from the work of Rhee [29]. The dimensions of the cuboidal tank are 1200 mm, 600 mm, 300 mm in the x, y and z directions, respectively. 20% of the tank volume is filled with water and is subjected to a sinusoidal translation motion with an amplitude 0.06 m and time period 1.94 s along the x-direction. Pressure is monitored at three locations on the bounding walls of the tank, as shown in the Figure 3.1.

In the simulation setup, the convection terms are discretized using the second order

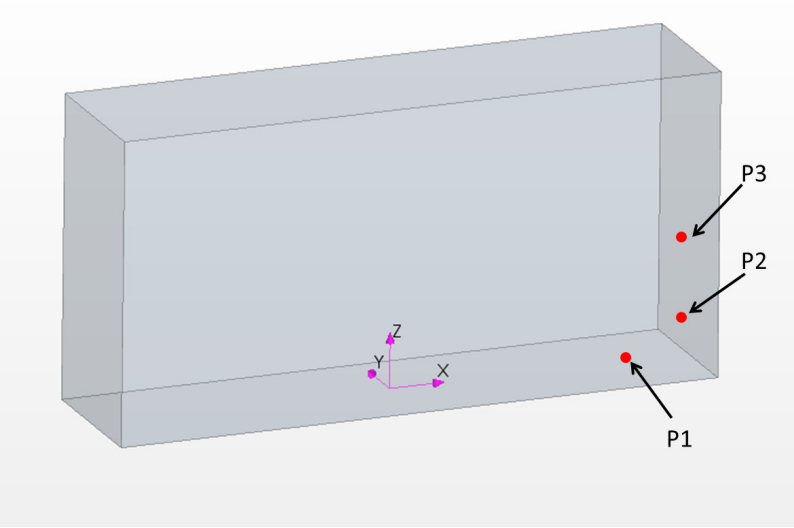

Figure 3.1: Tank geometry with pressure probes for CFD model validation

upwind scheme, the diffusion terms using second order central differencing scheme and the temporal term using second order implicit scheme. The time step is chosen as 0.001 s and the simulation is run for 12 s, corresponding to 5 sloshing impacts on the right wall. Hexahedral mesh was chosen for the simulations. With this time step and mesh configuration, an average Courant number, in both the interface and the entire domain, is always less than 0.5, as shown in Figure 3.2. This ensures the predominant implementation of the second order HRIC scheme, as described in subsection 2.1.1.

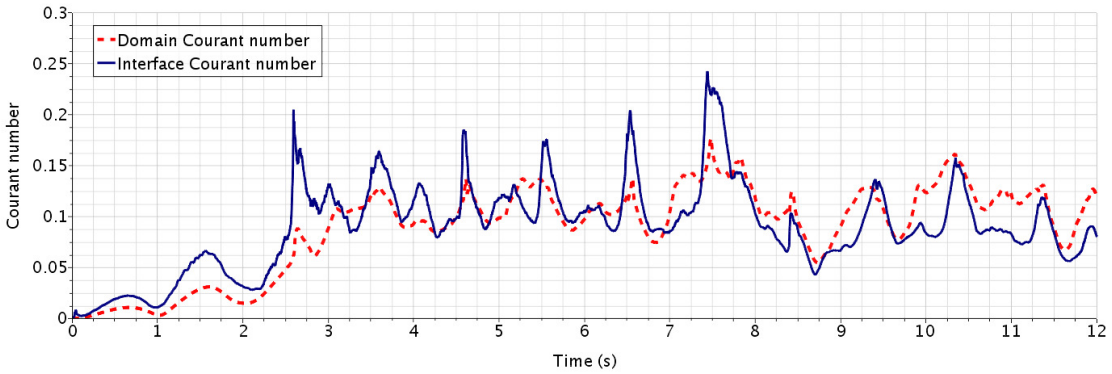

Figure 3.2: Volume averaged Courant number for the water-air interface (defined as water volume fraction between 0.01 to 0.99) and the entire domain. Note that the average Courant number is always below 0.5.

Locations of the pressure reference point and reference altitude are significant for obtaining correct pressure values for VOF simulations in STAR-CCM+. It is recommended to have the pressure reference point unhindered by the sudden changes in volume-fraction. To this end, the pressure reference points are located in a separate region vertically above and detached from the main tank domain, as followed

by Vaishnav, et al. [10]. Also, the reference altitude was placed at the initial free surface, as a datum for the hydrostatic pressure component.

Two different approaches are followed to simulate sloshing:

a. *Moving Mesh*: The translation motion is prescribed to the entire domain that moves the grid vertices according to the sinusoidal excitation. The grid velocities are accounted for in the governing equations. For example, the incompressible continuity equation with grid velocity, v^g, is written as

$$\frac{\partial(v_i - v_i^g)}{\partial x_i} = 0 \tag{3.1}$$

This rigid body motion of the tank results in liquid sloshing. Thus, this method represents a direct way of simulating sloshing phenomenon.

b. *Momentum Source Term*: The acceleration resulting from the aforementioned sinusoidal motion of the tank is provided as a momentum source term. The fluid experiences forces due to this acceleration in addition to acceleration due to gravity. Thus, this method represents an indirect way of simulating sloshing without having to move the tank by moving the mesh.

Figure 3.3 compares the pressure signals obtained through these two methods at the three pressure probes. Note that the time in the x-axis of the plots is non-dimensionalized with the time period of the sinusoidal excitation (T=1.94 s). The initial difference in the pressure signals in the plots is attributed to the time taken for the fluid to respond to the moving mesh in the first method. Nonetheless, the two approaches yield quite closely comparing results. This motivates the use of the second approach in that it is easier to implement and relevant for the simulation setup of the Volvo fuel tank since the acceleration signals from the test rig are available as input.

The above results were carried out on a two-dimensional domain (i.e., the xz plane in Figure 3.1), neglecting the width of the tank. However, comparisons were also made using a three-dimensional domain and similar results were obtained. Figure 3.4 shows the pressure signals for the two and three dimensional domains in comparison with the results in the aforementioned paper. In each of the five sloshing instances, the wall experiences first, a high pressure impact, followed by a secondary lower pressure impact. Except for the numerically induced noise in the three-dimensional domain, that has too high a frequency to affect the walls, the signals compare very well for both domains. This is attributed to the fact that the translation motion is prescribed in the x-direction only, and the effects of sloshing in the transverse direction are insignificant. In order to save computational time, only the two-dimensional domain has been used for further analysis in this section.

The effects of varying sharpening factor, C_α, in surface compression term (see Equation 2.7) are analyzed by monitoring the transient normalized domain mass (see Figure 3.5). Mass in each cell is given by

$$M_{cell} = \rho_{water}\alpha_{water}V_{cell} + \rho_{air}\alpha_{air}V_{cell} \tag{3.2}$$

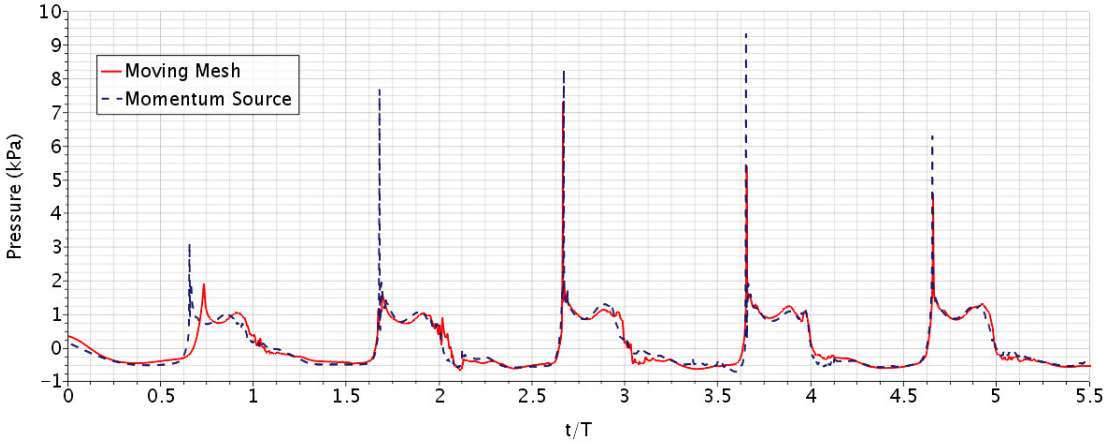

(a) Probe P1

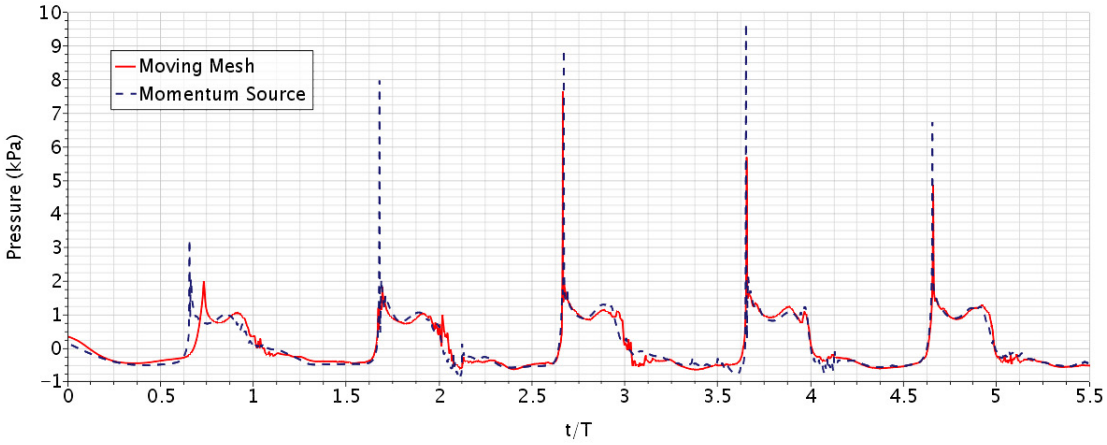

(b) Probe P2

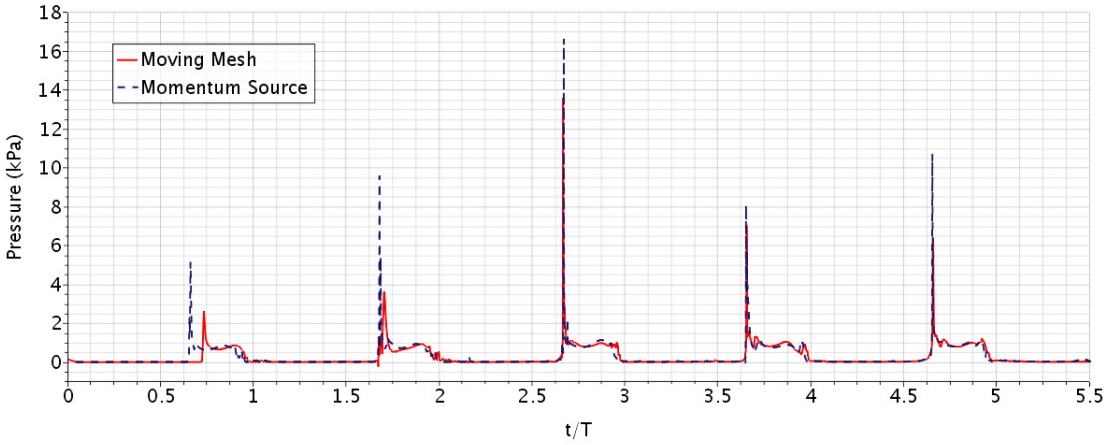

(c) Probe P3

Figure 3.3: Comparison of pressure signals at the three pressure probes for the *Moving Mesh* and *Momentum Source Term* approaches

Domain mass is the sum of masses of all the cells in the domain. For a numerically accurate method, the domain mass is expected to be conserved. Although changing C_α sharpens the water-air interface (Figure 3.6), it induces an artificial surface compression which gets compensated by the numerically induced mass, as seen in Figure 3.5. From Figure 3.7, it is seen that there is no significant gain in accuracy of pressure signals by increasing C_α. Thus, no sharpening factor is used to obtain a mass-conserved solution.

The sharp spikes observed at certain sloshing impacts in the pressure plots in Figure 3.3 and Figure 3.4 occur for a very small duration of 0.01 s, corresponding to 0.5 per cent of the excitation time period. These extremely high frequency pressure signals are purely numerical and are considered as noise. Such spikes are also observed in similar studies around sloshing analysis [16, 42, 43]. Moving average filters can be used to obtain physically-relevant continuous signals, as shown in Figure 3.8.

The model parameters from this validation are treated as basis for the coupled CFD-FEA methodology in all following simulations.

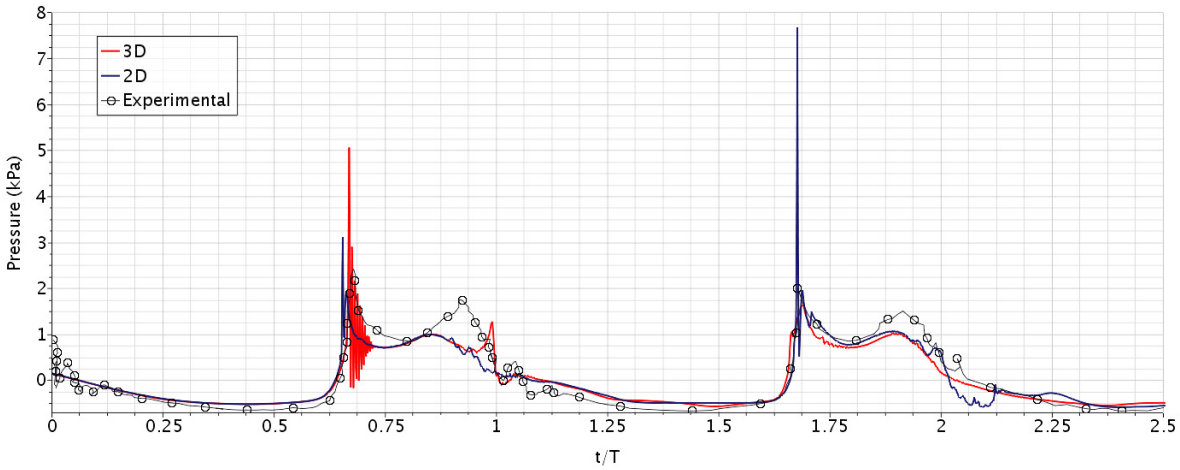

(a) Probe P1

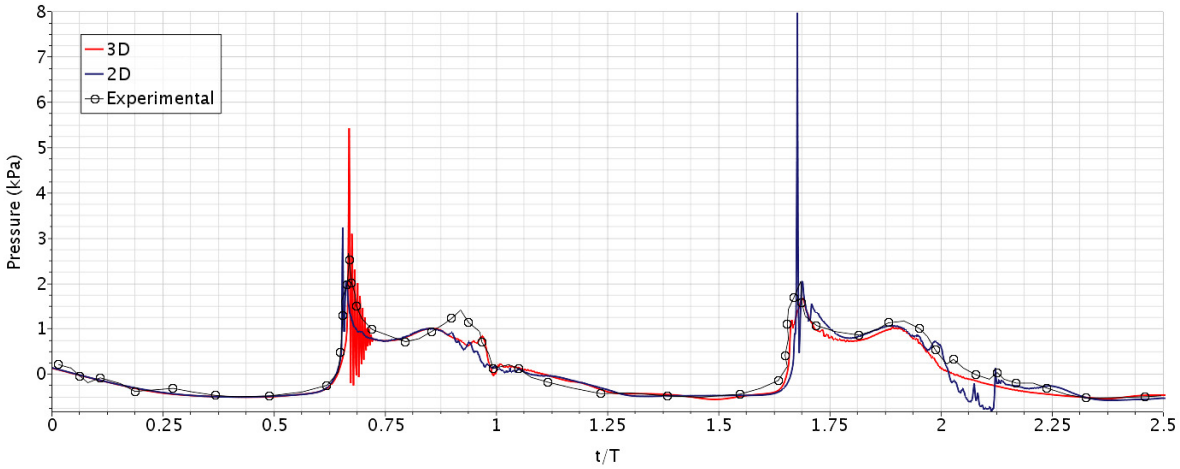

(b) Probe P2

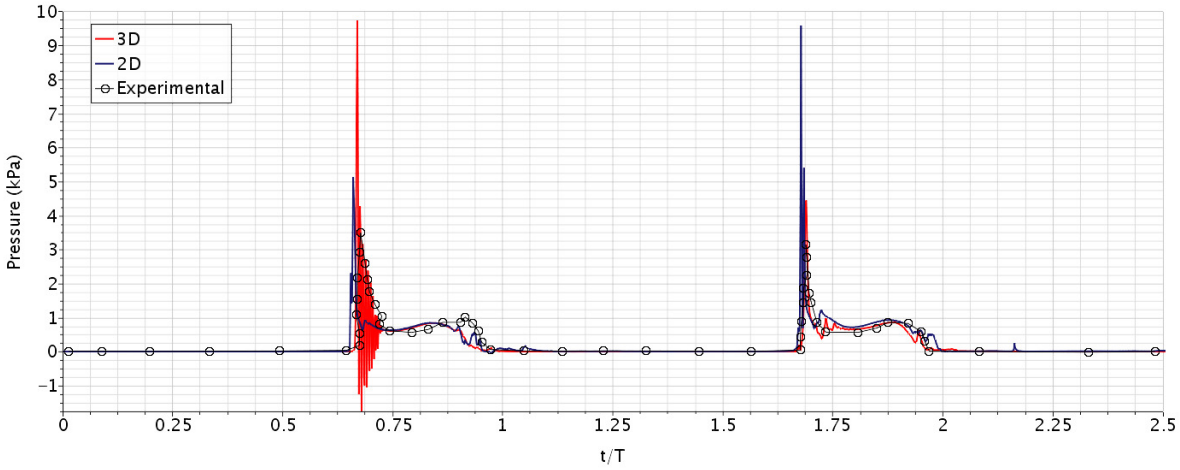

(c) Probe P3

Figure 3.4: Pressure signals at the three probes for the two and three dimensional domains in comparison with experimental data

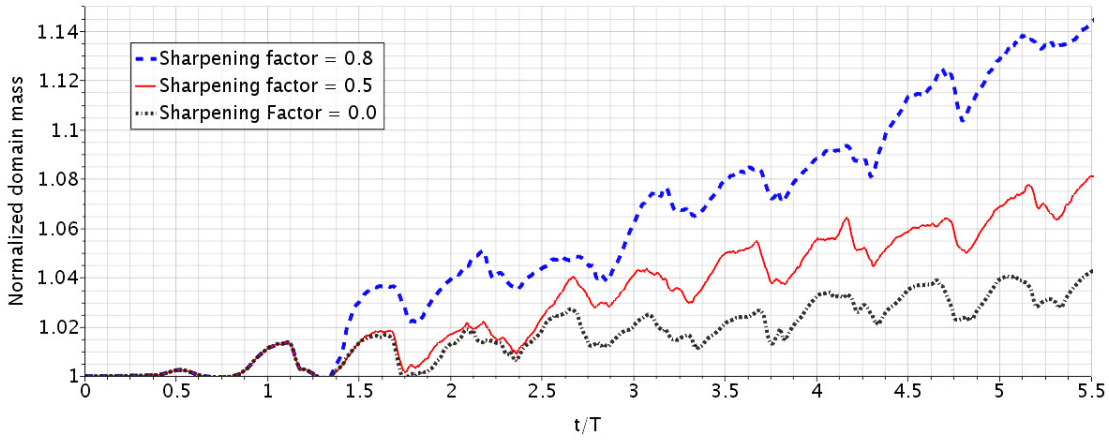

Figure 3.5: Domain Mass (normalized with the initial total mass) for varying sharpening factors, C_α. Clearly, an increase in the sharpening factor corresponds to an increase in the numerically induced domain mass.

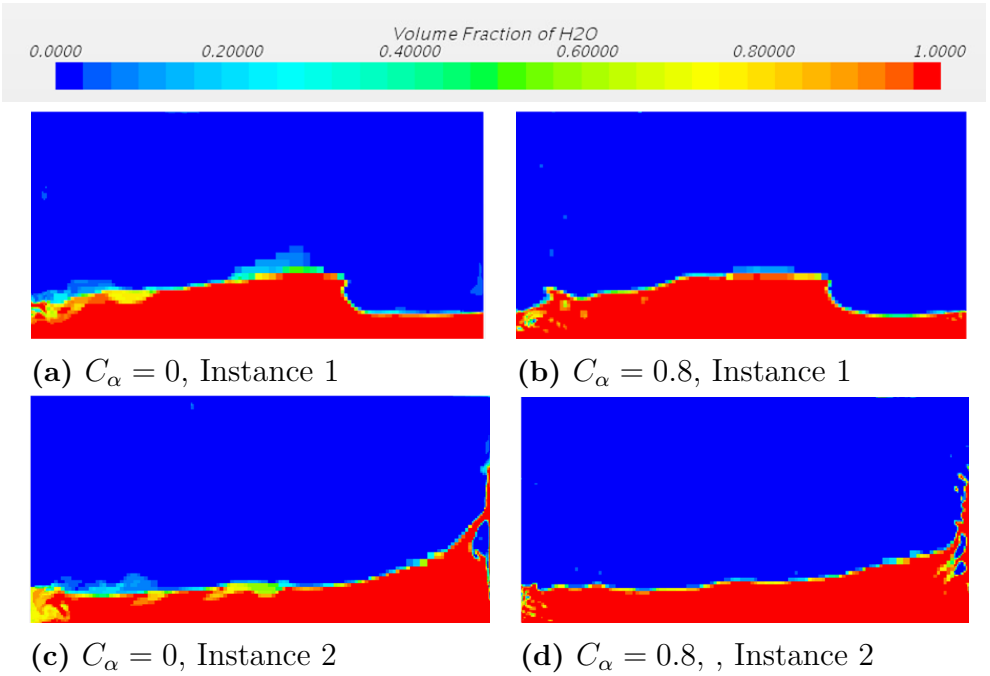

(a) $C_\alpha = 0$, Instance 1

(b) $C_\alpha = 0.8$, Instance 1

(c) $C_\alpha = 0$, Instance 2

(d) $C_\alpha = 0.8$, , Instance 2

Figure 3.6: Contours of volume fraction of water for $C_\alpha = 0$ and $C_\alpha = 0.8$ at two instances. Note the sharp interface in **(b)** and **(d)** owing to the increased C_α.

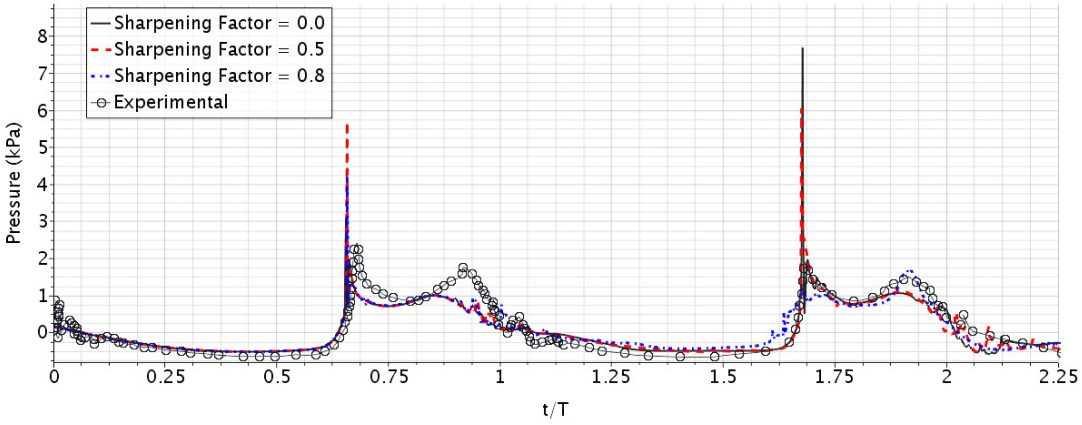

(a) Probe P1

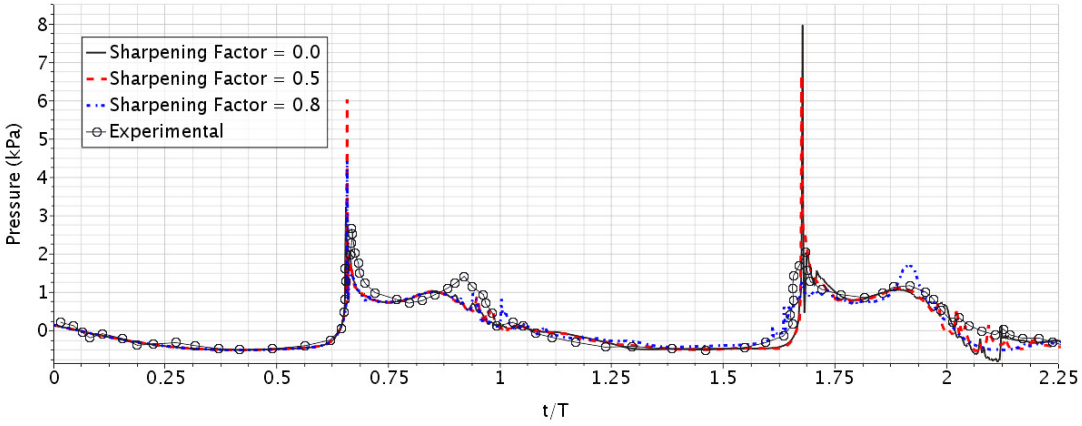

(b) Probe P2

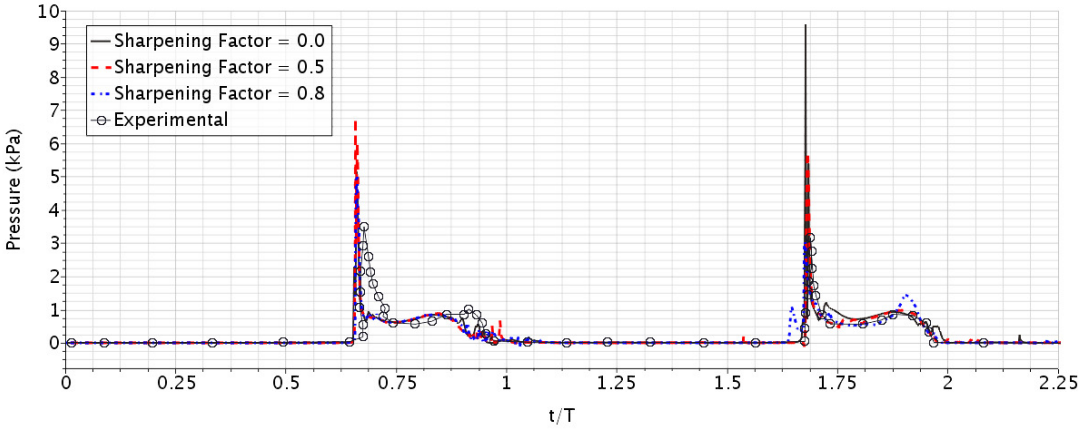

(c) Probe P3

Figure 3.7: Effect of sharpening factor on pressure signals

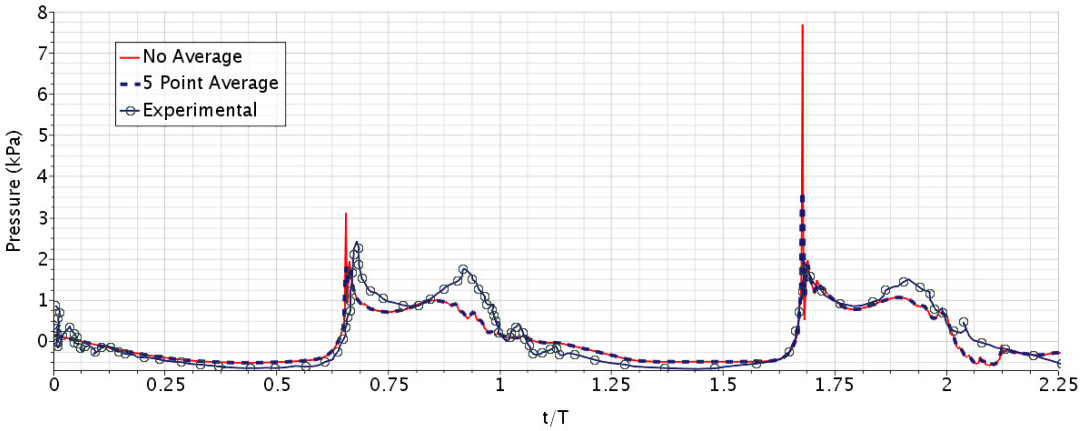

(a) Probe P1

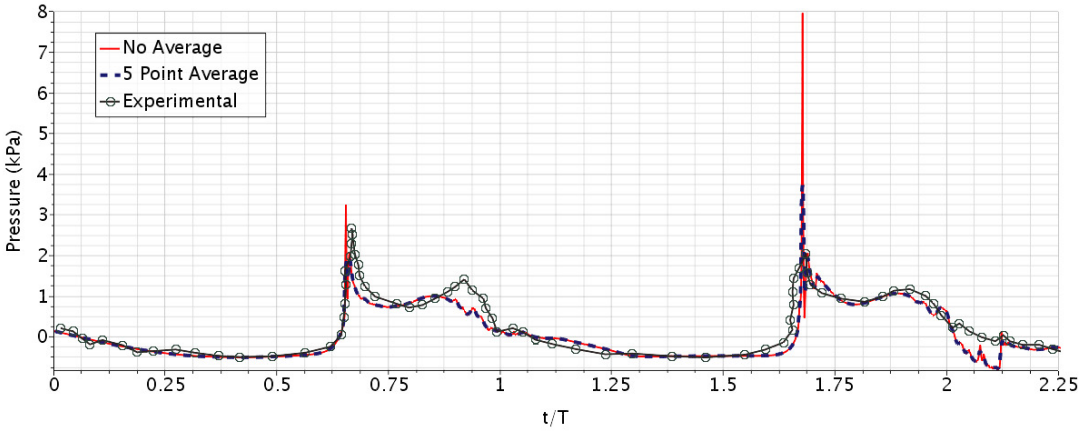

(b) Probe P2

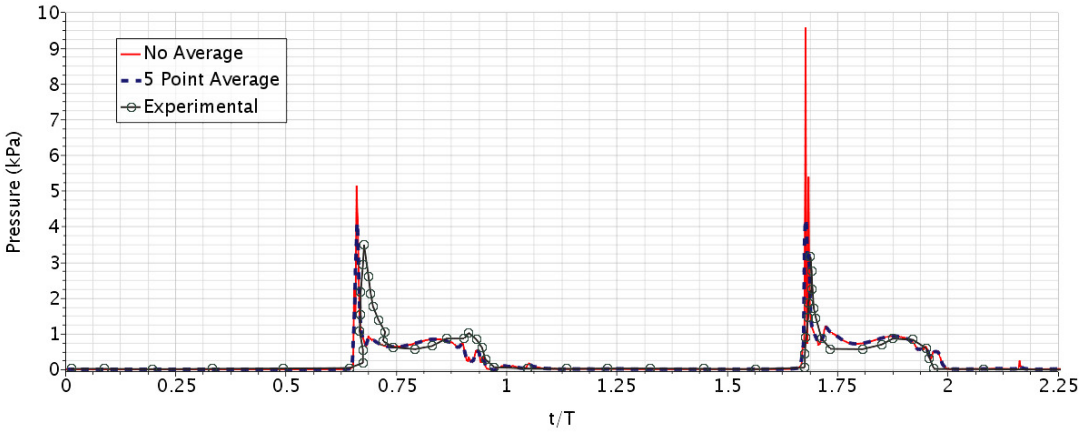

(c) Probe P3

Figure 3.8: Comparison of pressure signals with experimental and filtered (using a moving window average) pressure signals. Clearly, the use of moving average filters out the high frequency spikes, while retaining the overall dynamic response.

3.1.2 Fluid-Structure Interaction

Further to validation of the VOF model in STAR-CCM+, an elastic baffle is introduced at the bottom of the tank described in subsection 3.1.1 (see Figure 3.9) to study the effects of fluid-structure interaction. The tank is subjected to the same sinusoidal excitation (amplitude = 0.06 m, time period = 1.94 s). Assuming the walls of the tank to be rigid, the baffle is the only flexible member in the tank structure. The dimensions of the baffle are 5 mm, 150 mm and 120 mm in the x, y and z directions, respectively. The material of the baffle has a density of 4096 kg/m^3, young's modulus of 38.4 MPa and poisson's ratio of 0.3. The study is performed using a) the FSI module within STAR-CCM+ and b) by coupling the CFD solver in STAR-CCM+ with the FEA solver in Abaqus. The displacements at the top of the baffle and the pressures at locations defined in the VOF validation study are monitored and compared for the two approaches. The respective displacement and pressure probes are also highlighted in Figure 3.9.

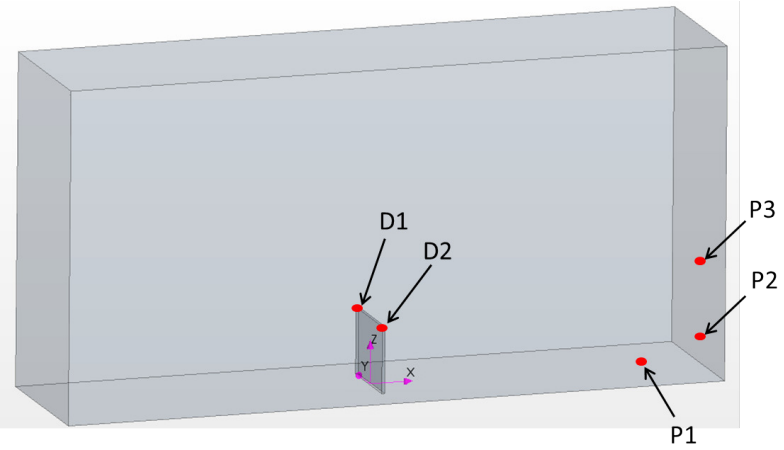

Figure 3.9: Tank geometry with added flexible baffle

For the FSI analysis within STAR-CCM+, the second order accurate implicit unsteady and linear elastic isotropic solid stress models are chosen to solve the solid domain (baffle) using the FEA approach. The fluid-structure coupling model is used to perform the FSI analysis. The baffle is meshed using linear hexahedral elements with 8 nodes and its bottom is constrained to prevent rigid body motions. The models chosen for solving the fluid domain are retained from the VOF validation study. The displacement field of the solid region is mapped at the fluid-solid interface; the fluid domain is then morphed in accordance with this displacement. The mesh morphing is performed at every inner iteration, since it is a strongly coupled problem. A common time step of 0.001 s is used in solving the problem.

In the STAR-CCM+ Abaqus coupled simulation approach, the co-simulation engine (CSE) API is used. This API handles the mapping of the exchanged traction (pressure + wall shear stress) and displacement fields between the solid and fluid domains. The solid mesh for both FSI approaches is kept the same. For the solid

domain, a dynamic analysis with implicit time integration scheme is chosen with a time increment of 0.001 s. The fields are exchanged between the solid and fluid solvers at every inner iteration within a time step.

Figure 3.10 shows the pressure at points P1, P2 and P3 with and without the baffle. Clearly, the peak impact pressures were reduced due to presence of the baffle. However, an increase in pressure during the time intervals between the impacts is also observed caused by the increased hydro-static pressure due to the fluid contained between the baffle and the walls.

Further, results from the aforementioned approaches for the FSI analysis are compared. The x-displacements at D1 and D2, as shown in Figure 3.11, clearly compare the performance of the solid FE solvers. The displacement computed by Abaqus is greater in magnitude than the one by the FE solver in STAR-CCM+. The difference is pronounced only for the maximum bending of the baffle (magnitudes of displacements greater than 20 mm). However, for smaller displacements, results from the two solid solvers are in close agreement. This small difference in displacements in the two approaches is considered an acceptable trade-off for the high computational expenses incurred in coupling STAR-CCM+ and Abaqus using the CSE API.

The FSI analysis methodology is validated with numerical and experimental results based on the benchmark studies on flexible baffles in sloshing flows by Idelsohn et al. [44]. These experiments were conducted on a rectangular prismatic tank with clamped elastic beam, filled with sunflower oil. One of the three test cases of the aforementioned work is chosen for this validation study. The tank is 609 mm long, 344.5 mm high and 39 mm wide. The flexible beam clamped to the bottom of the tank has dimensions 4 mm, 33.2 mm and 57.4 mm in x, y and z directions. The flexible beam made of dielectric polyurethane, has a density of 1100 kg/m^3, Young's modulus of 6 MPa and Poisson's ratio of 0.4. Oil is filled in the tank up to the height of the beam. The density and kinematic viscosity of sunflower oil are 917 kg/m^3 and $5e-5$ m^2/s, respectively. The tank is subjected to sinusoidal oscillatory motion about the y-axis, with amplitude 4 degrees and frequency 0.61 Hz.

Numerical simulations for this setup are performed using FSI capabilities within STAR-CCM+. Both fluid and solid solvers have been set-up as described in the previous sections. The domain is subjected to mesh motion due to the simultaneous effect of prescribed rigid body oscillatory motion and fluid-structure interaction. Figure 3.12 shows the comparison of displacements at the tip of the baffle obtained in the present study with those in Idelsohn et al. It is seen that the results compare fairly well with the existing experimental and numerical data. It is to be noted that there is an initial 0.3 s mismatch in the excitation signal of the current study and that in Idelsohn et al. The displacement plots are therefore appropriately offset. The initial deviation is attributed to this offset.

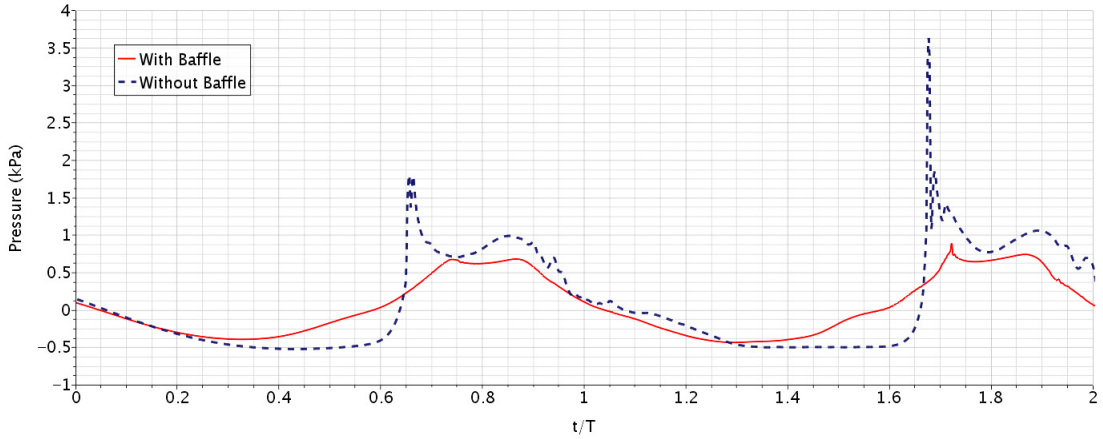

(a) Probe P1

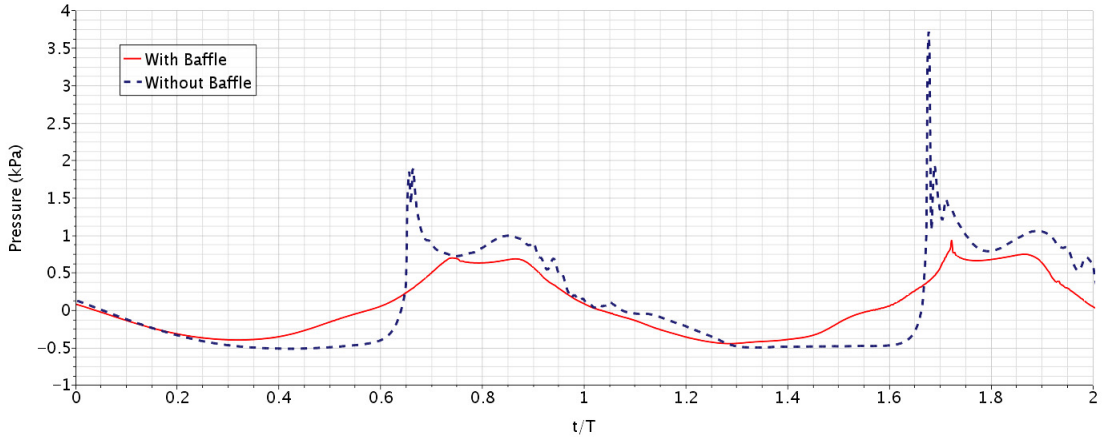

(b) Probe P2

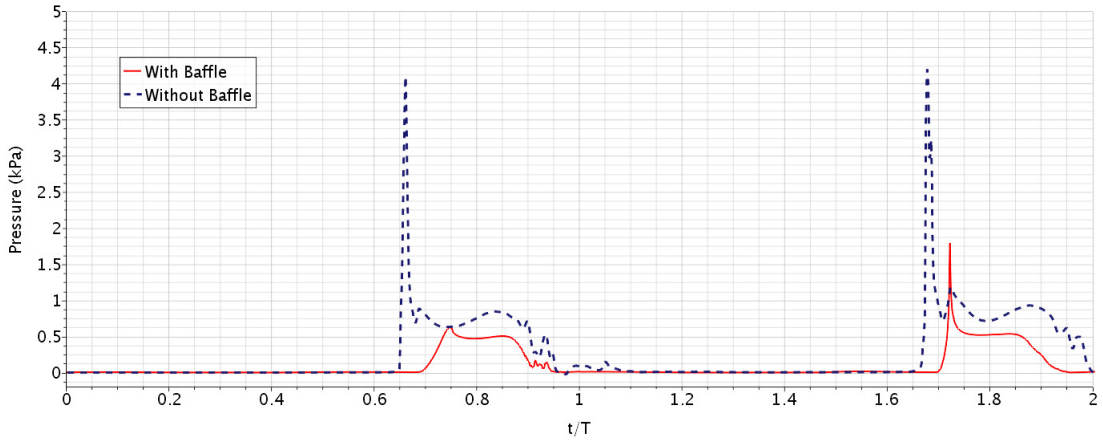

(c) Probe P3

Figure 3.10: Comparison of pressures with and without the baffle in the rectangular tank. Clearly, the impact pressures at the probes decrease with addition of the baffle.

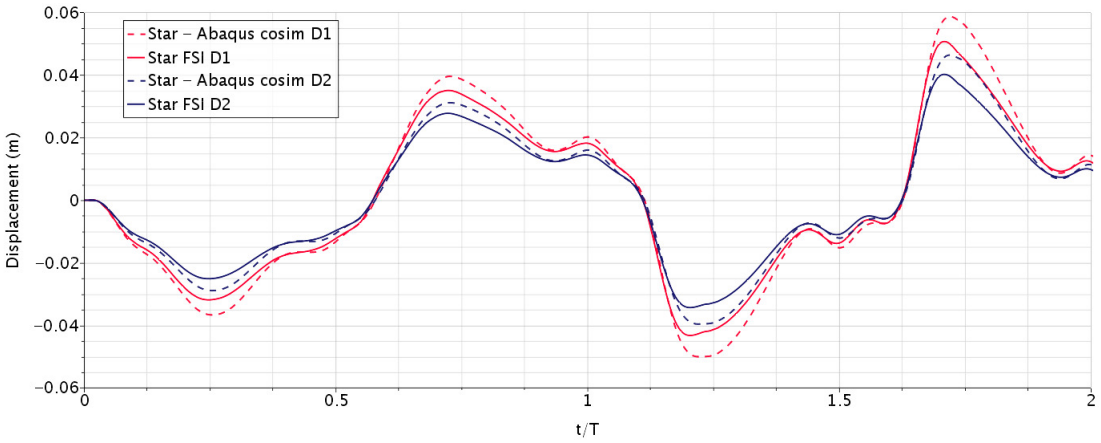

Figure 3.11: Comparison of baffle-tip displacements from the two FSI simulation approaches. The difference between the two approaches gets pronounced at instances of maximum bending of baffle.

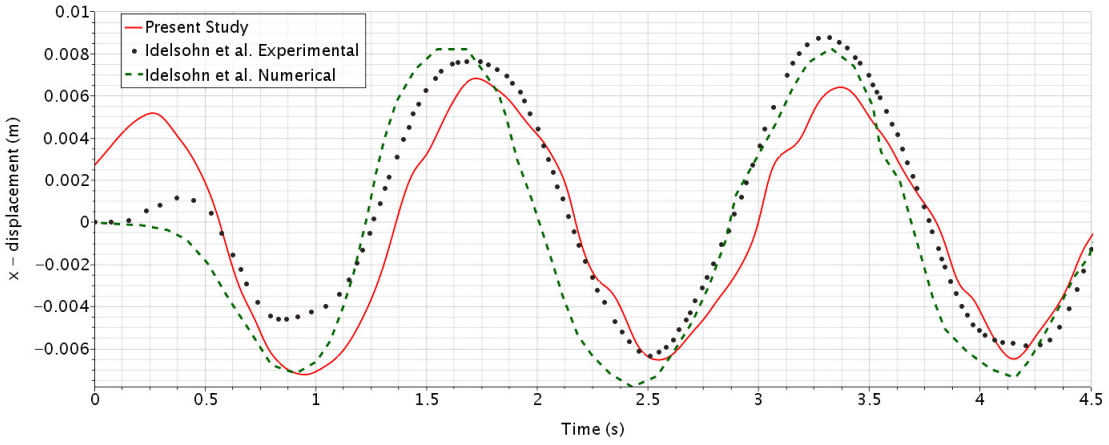

Figure 3.12: Comparison of displacements obtained in the present study with experimental and numerical results in [44]

3.2 Simulation Setup

3.2.1 Volvo Fuel Tank

Figure 3.13 shows the geometry of a 450 L D-shaped Volvo fuel tank, commonly used in series FH, FM and FMX trucks. The tank is 1.03 m long and 0.71 m high. The walls and baffles are made of 2.5 mm thick Aluminum plates. It is supported with belts that wrap around the welds close to the baffles. These belts are connected to brackets that secure the tank to the main frame of the truck. For simulations in this study, these belts are constrained to prevent any rigid body motion of the tank, as shown in Figure 3.14.

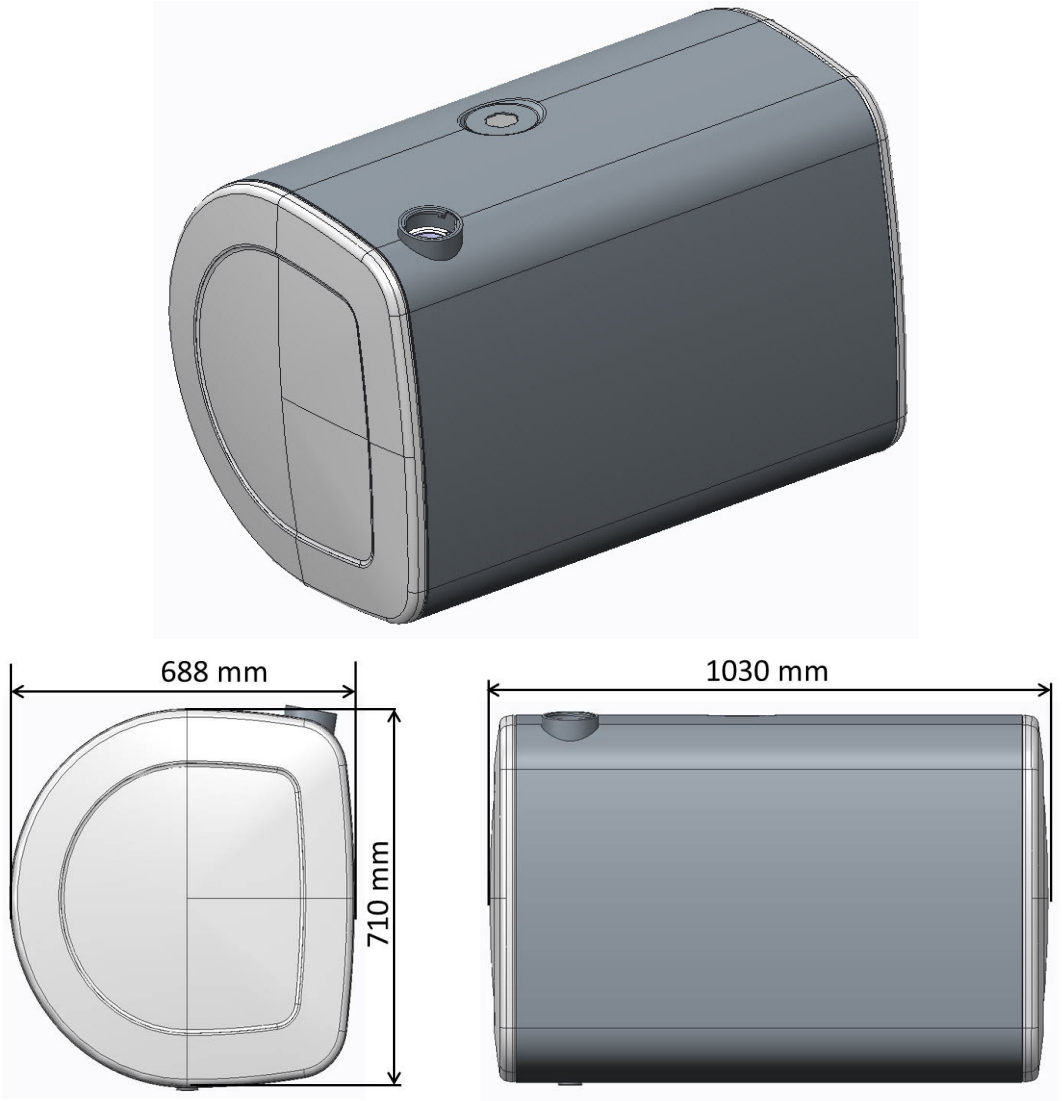

Figure 3.13: CAD model of the 450 L D-Shaped Volvo Fuel Tank

For the numerical analyses, CAD clean-up and a preliminary surface mesh is prepared in ANSA for further refinement and volume meshing in STAR-CCM+. Polyhedral cells with prism layers are used for volume meshing, as shown in Figure 3.15.

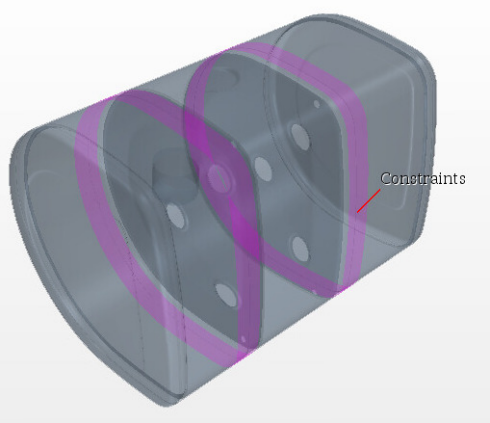

Figure 3.14: Fuel tank model highlighting the constrained surfaces

The solid region is meshed with tetrahedral cells. Figure 3.16 shows the non-conformal meshes of the fluid and solid regions. The model setup for the fluid and solid domains is derived from the previously described validation studies. The fluid mesh sensitivity analysis using the VOF model is performed to achieve grid-independent results and the resulting mesh is used for the concomitant FSI analyses. Studies for varying fill levels (20%, 40%, 60% and 80% by volume) are conducted for one-way and two-way coupled FSI analyses.

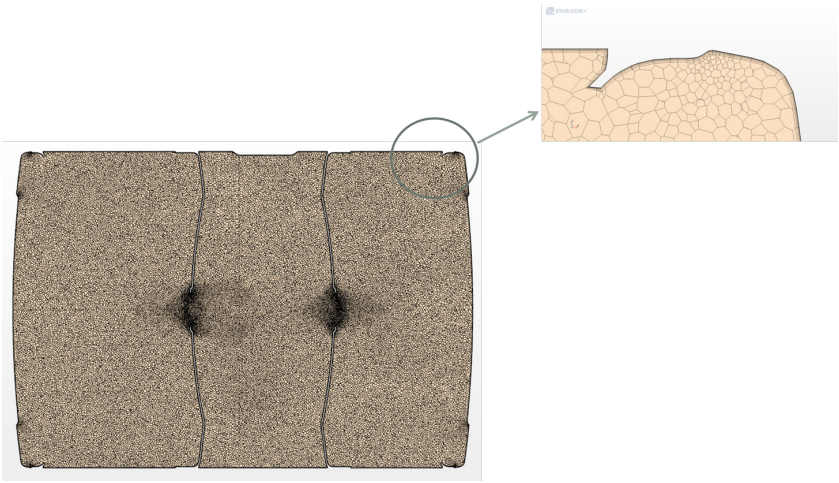

Figure 3.15: Sectional view showing the fluid region meshed with polyhedral cells and prism layers

Fuel sloshing is simulated with input acceleration signals using the Momentum Source Terms method as described in subsection 3.1.1. The acceleration signals corresponding to each fill level from one of the sensors positioned at the end plates of the tank were used. These signals were recorded during the proving track lap runs through obstacles of different topologies for tanks filled different fill levels (see Figure 3.17). The same signals were replicated in the shake-tests conducted at Volvo GTT. The test rig consists of actuating pistons driven by the acceleration signals recorded at the proving track. Figure 3.18 shows the experimental setup to measure the in-plane strains at the walls of the fuel-tank. There are two acceleration sensors

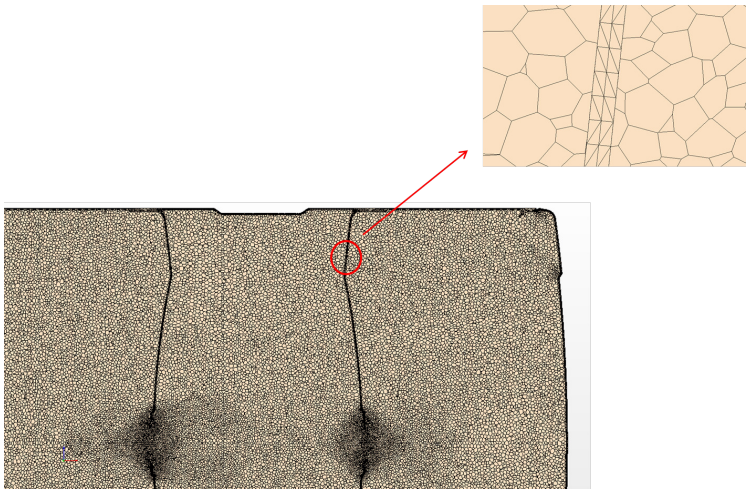

Figure 3.16: Sectional view showing the non-conformal fluid and solid domain meshes. The magnified view shows the polyhedral cells in the fluid region and the tetrahedral cells of the solid region.

on the front and rear of the tank and four strain gauges — three on the front end wall and one on the rear. Since these strain gauges cover a small area (and not just a point) of the tank surface, the experimental result for each strain gauge is compared by taking the mean of three closely placed strain probes in the simulations. Owing to the prohibitively high computational costs in simulating the entire test track, signals causing the most severe (low frequency, high amplitude) excitation were considered for the analyses. These correspond to the *out-of-phase washboard* obstacle. The acceleration signals for a 40% filled tank are included in the appendix (Figure A.1).

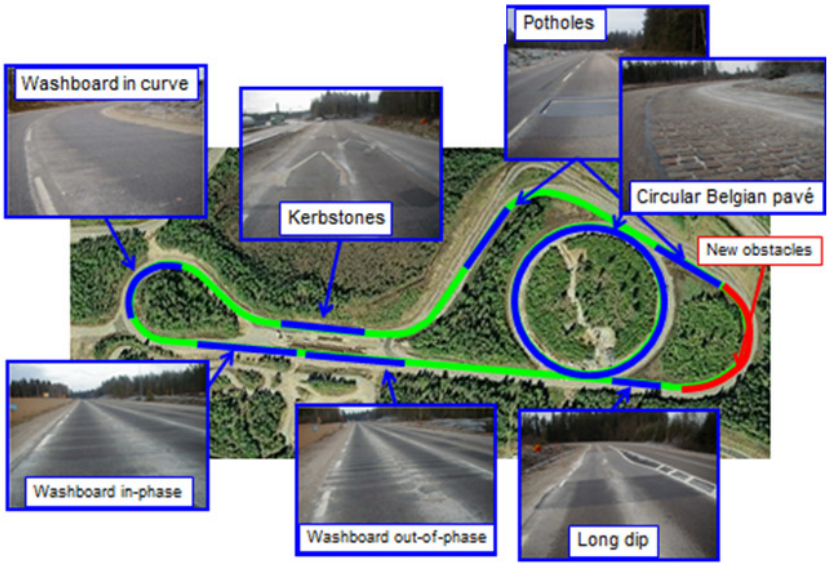

Figure 3.17: Test track with different obstacle topologies. Acceleration signal from *Washboard out-of-phase* represents the worst case scenario for fuel sloshing and is chosen for analysis in this study.

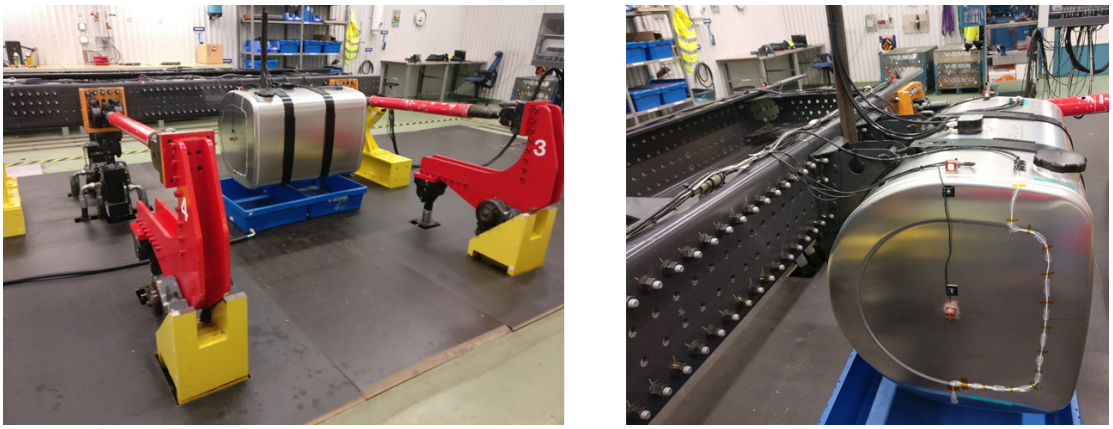

Figure 3.18: Test rig for experimental investigation of fuel tanks at Volvo

3.2.2 Representative Tank

Since the geometry, as well as the acceleration signals, is complicated, a simplified model (Figure 3.19) is created that captures the essential geometric features of the Volvo fuel-tank. The dimensions of the tank are 1.2 m, 0.3 m and 0.6 m in the x, y and z directions, respectively with the baffles placed at a distance of 0.3 m on either side of the origin along the x-axis. The tank is subjected to sinusoidal excitation, as in subsection 3.1.1 and the resulting periodic sloshing facilitates a clear interpretation of the results, while keeping the computational expenses minimal. Along with the Volvo tank, studies conducted for this geometry give a holistic perspective on the underlying physics. The results of the simplified tank and the Volvo fuel tank are discussed in the following chapter.

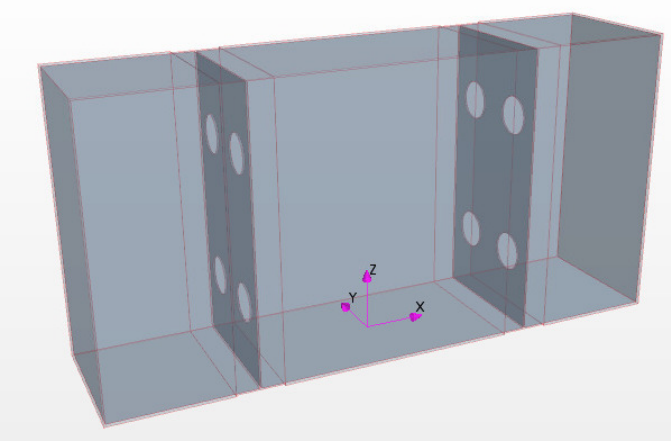

Figure 3.19: Representative tank model

4
Results

In this section, the results obtained from the FSI analysis of the simplified representative tank and the Volvo fuel tank are discussed. For the Volvo fuel tank, a detailed discussion pertaining to mesh sensitivity analysis is first presented. This is followed by comparison of the results obtained from the one-way and two-way coupled FSI simulations with the experimental tests.

4.1 Representative Tank

As discussed in section 3.2, the FSI analysis is performed on a simple tank model with important geometric features of the Volvo fuel tank and is subjected to sinusoidal excitation. The meshing strategy for this simplified model is similar to that of the Volvo tank and consists of 0.75 million polyhedral cells in the fluid region and 0.51 million tetrahedral cells in the solid region. The simulations are performed for the fill levels of 20%, 40%, 60% and 80% by volume.

To start with, the sinusoidal excitation gives a clear picture of the effect of sloshing impacts on the tank structure. Figure 4.1 shows contours of volume fraction of water at a sloshing instance and the corresponding displacement (deformation) at the end walls and baffles. Further, Figure 4.2 shows trends of increasing pressure on the tank wall resulting from increasing fill levels. Taking a closer look at the pressure signals, a lot of high frequency impacts (wiggles) are observed for the 80% filled tank. This can be attributed to the free surface waves affected by the upper set of holes in the baffles for this fill level. For other fill levels, the water level does not reach the upper holes in the baffle, and the pressure signals therefore remain smooth. This effect is further clear by monitoring the displacements at a couple of locations on the baffles and end walls. Clearly, from Figure 4.3 and Figure 4.4, the root mean squared (RMS) displacements increase with increasing fill levels at the end wall, while there is a sharp decrease corresponding to 80% filling at the baffles. The top holes provide an outlet to the sloshing waves, thereby reducing their impact on the baffles and leading to this decrease in the displacements. Thus, the results from these simulations give important insight into some characteristic features of liquid sloshing and the associated fluid-structure interactions.

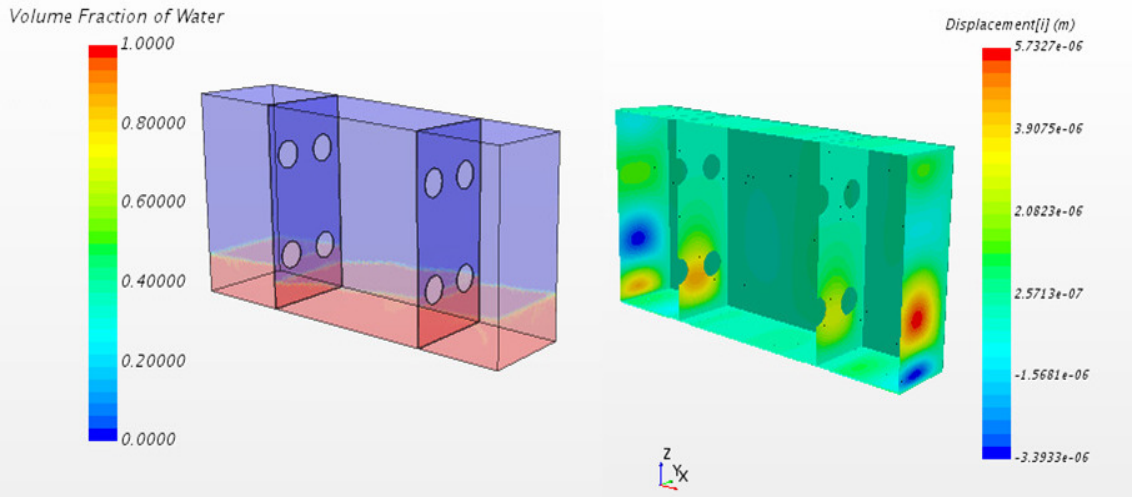

Figure 4.1: Contours of water volume fraction and corresponding x-displacement of the solid domain. High displacements can be seen on the right end wall when the fuel is sloshing towards the right.

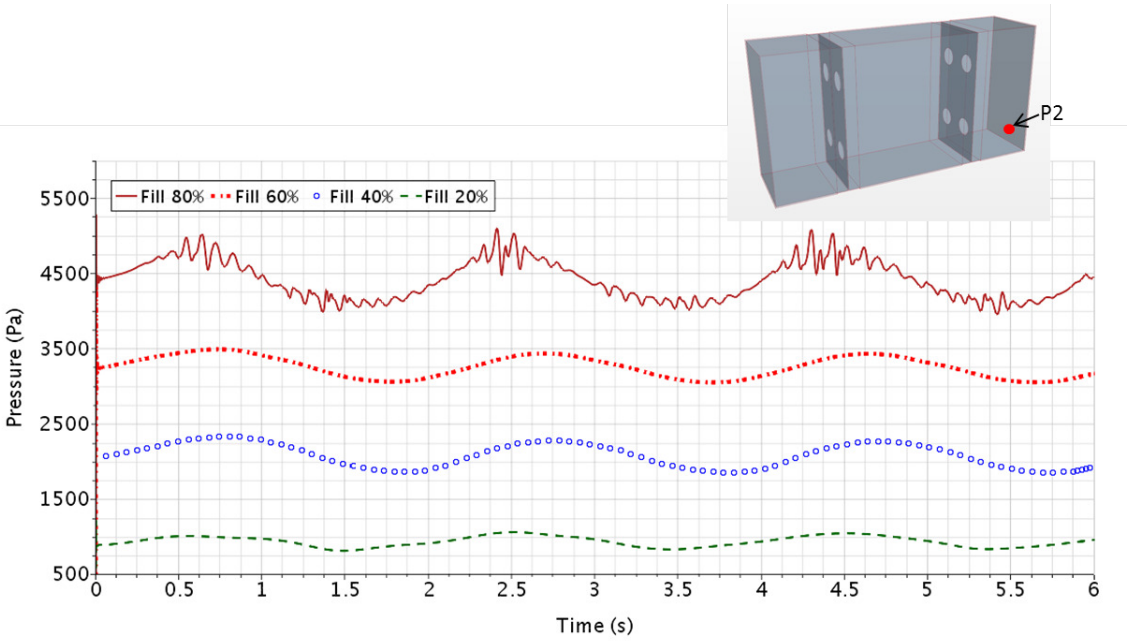

Figure 4.2: Pressure signals at the right wall for different fill levels.

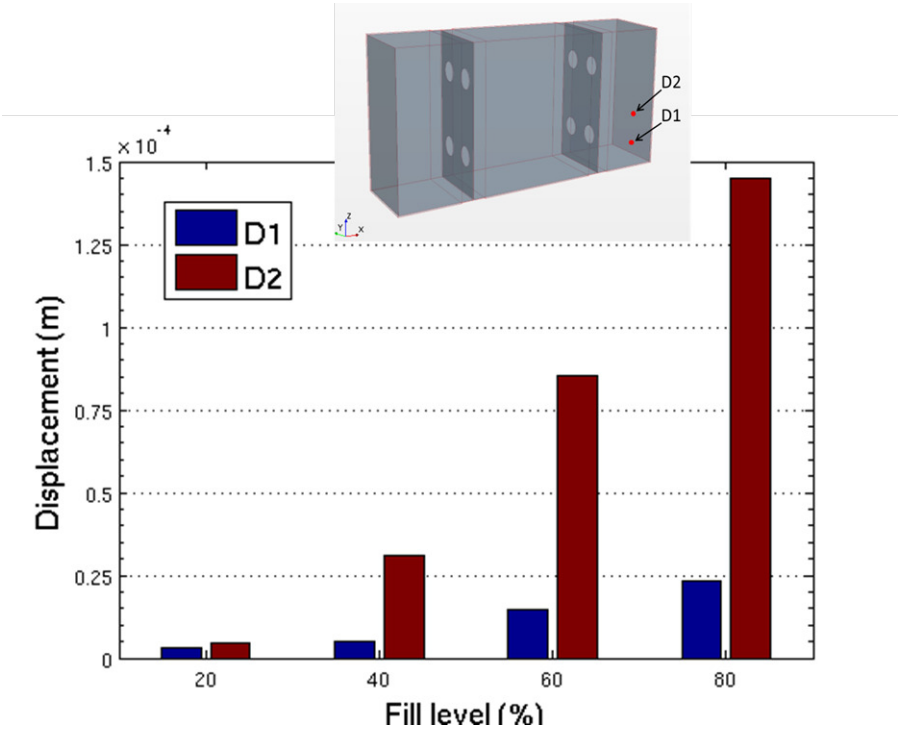

Figure 4.3: RMS displacements on the bounding wall for varying fill levels

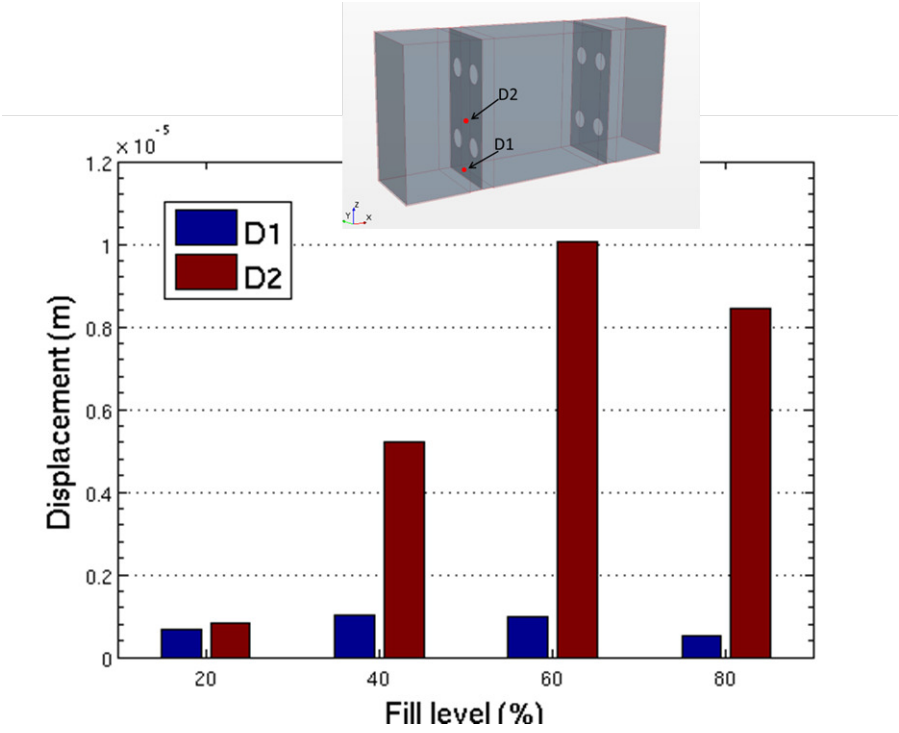

Figure 4.4: RMS displacements on the baffle for varying fill levels

4.2 Volvo Fuel Tank

4.2.1 Mesh Sensitivity Analysis

Firstly, a mesh sensitivity study is performed to obtain grid independence for the volume mesh of the fluid region. The fluid domain is meshed with polyhedral cells and prism layers at the walls. The mesh is refined in vicinity of the holes in the baffles. Five mesh configurations are obtained by altering the base size of the polyhedral cells and CFD simulations with VOF model are performed on these configurations. The simulations are performed for a period of 2 s with a time step of size 0.001 s. The tank is filled 40% by volume with water and is subjected to acceleration signals, corresponding to the out-of-phase washboard obstacle at the Volvo proving track. Surface averaged pressure on one of the baffles is monitored and its RMS value is used as a parameter for obtaining grid independence. Figure 4.5 shows the variation of this parameter for the five mesh configurations and the final mesh configuration (with 11.05 million cells) chosen for further analysis is highlighted.

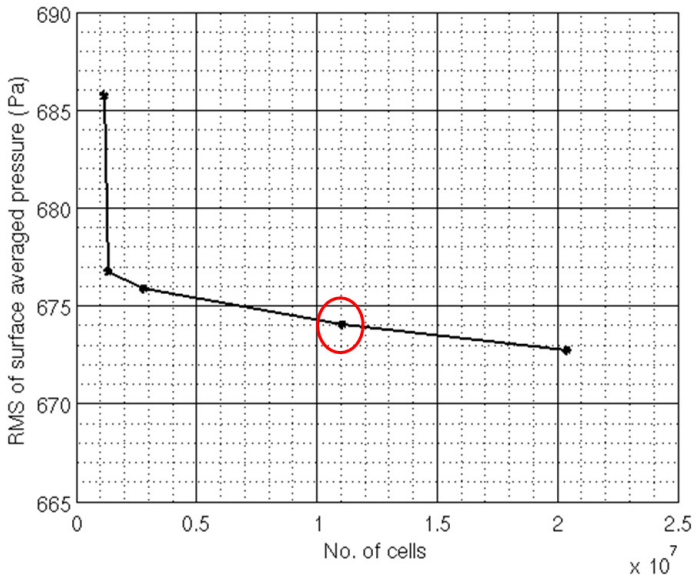

Figure 4.5: Grid independence study based on root mean squared surface averaged pressures

Further, the time step size is fine tuned to enhance the accuracy of the results. To this end, the percentage of cells that have values of Courant number more than one are monitored for the aforementioned five mesh configurations, as shown in Figure 4.6. It is observed that for the chosen mesh configuration, on an average more than 1% of the cells have Courant number exceeding one. In order to minimize this, the time step size for the simulation was reduced to 0.0005 s. As illustrated in Figure 4.7, the number of cells with Courant number greater than 1 has reduced significantly by reducing the time step.

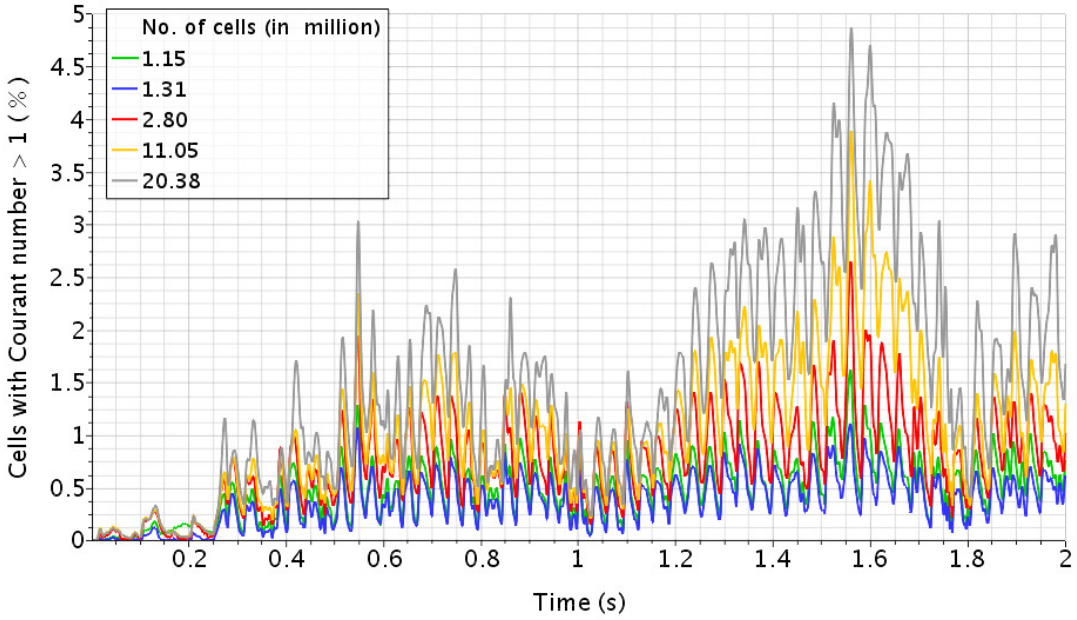

Figure 4.6: Percentage of cells with Courant number greater than 1 for the five mesh configurations. Clearly, the chosen mesh (with 11.05 million cells) has about 1% - 4% cells with Courant numbers greater than 1.

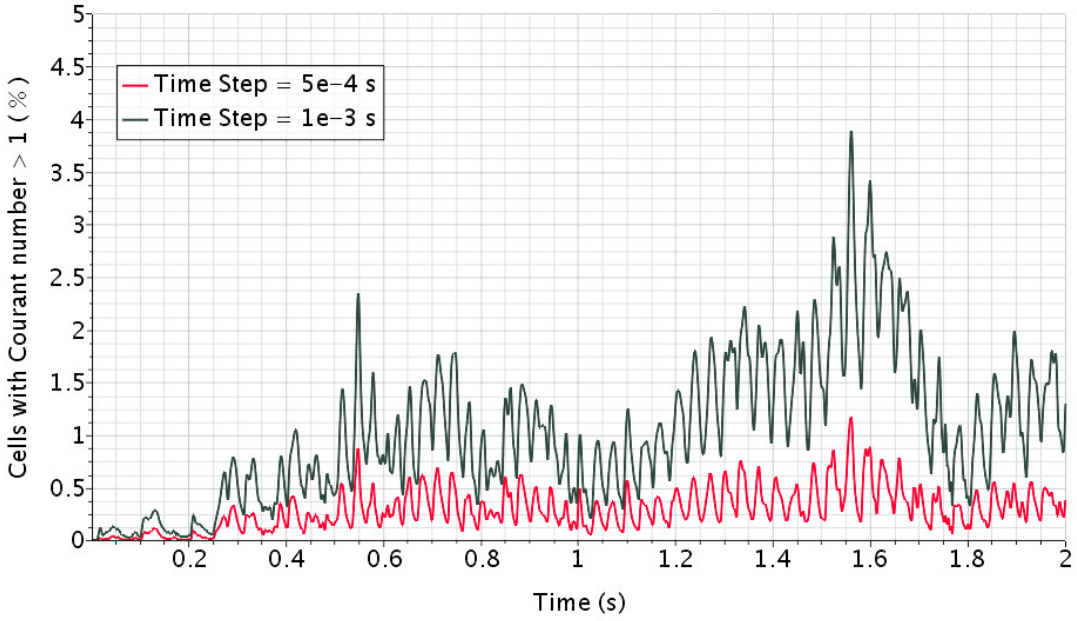

Figure 4.7: Effect of time step size on the percentage of cells with Courant Number greater than one. There is a sharp decrease in the percentage of cells with Courant number more than one upon reducing the time step.

Since the tank domain is subjected erratic excitation in all three co-ordinate directions, it is suspected that boundary layer development and hence, the wall resolution might be insignificant for this analysis. Therefore, the effects of removing the prism layers in the mesh are analyzed. As shown in Figure 4.8, it is seen that the percentage of cells in the interface decreases by removing the prism layers, resulting in an accurately captured interface. Figure 4.9 provides a visual confirmation of the reduction in the number of cells in the water-air interface. Since removal of the prism layers does not affect the surface averaged pressures and leads to a reduction in the total numbers of cells (and hence, the computational time), this mesh configuration is used for the simulations ahead.

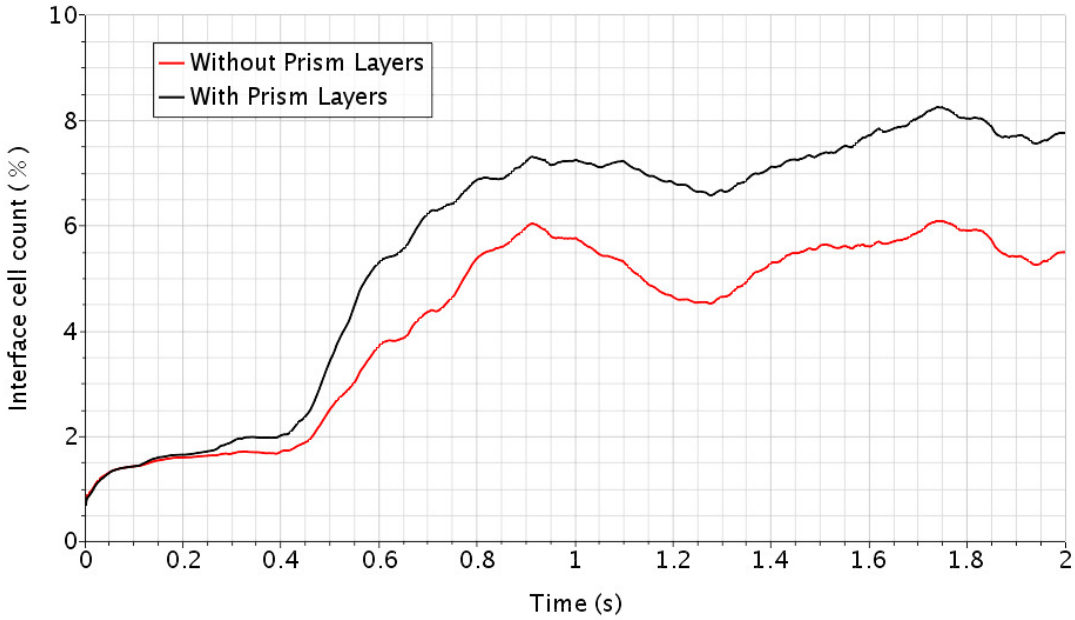

Figure 4.8: Percentage of cells in the water-air interface (defined as water volume fraction between 0.01 to 0.99).

Finally, the mesh for the fluid region consists of 8.28 million polyhedral cells having no prism layers. This, in combination with a time step size of 0.0005 s, keeps the cell Courant number lower than 0.5 and ensures a predominant implementation of the second order accurate HRIC scheme, as seen in Figure 4.10. The solid region is meshed with 0.56 million tetrahedral FE cells and this configuration is chosen for the subsequent FSI analysis.

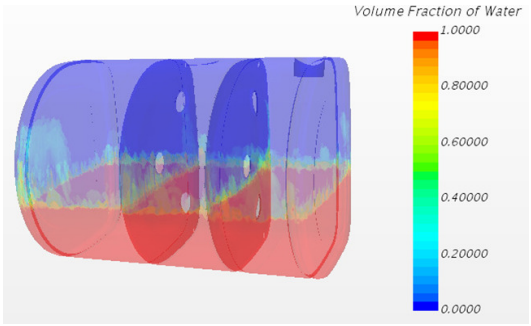

(a) with prism layers, at $t = 1.25\ s$

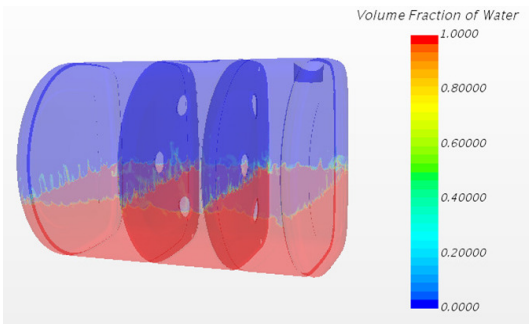

(b) without prism layers, at $t = 1.25\ s$

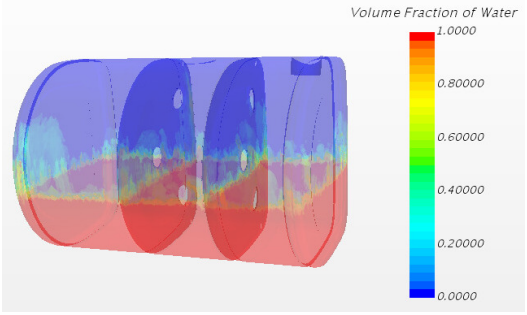

(c) with prism layers, at $t = 1.75\ s$

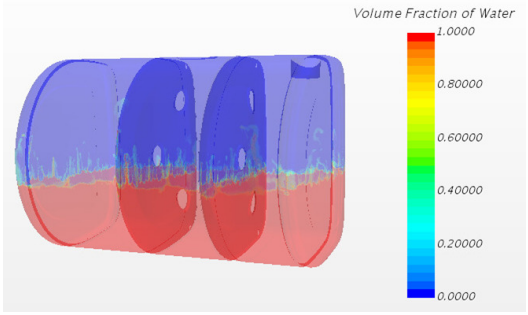

(d) without prism layers, at $t = 1.75\ s$

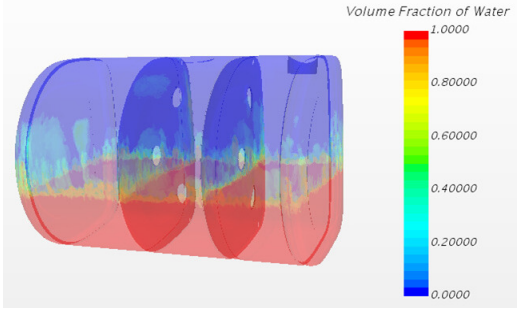

(e) with prism layers, at $t = 2\ s$

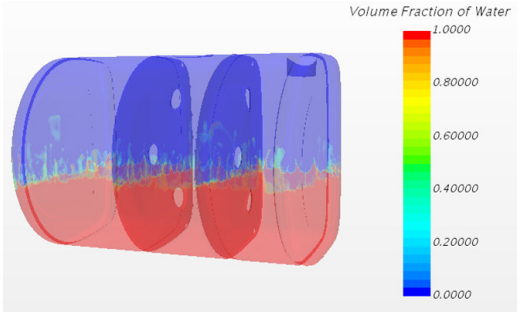

(f) without prism layers, at $t = 2\ s$

Figure 4.9: Comparison of contours of volume fraction of water at various instances, with and without prism layers. Clearly, removing the prism layers results in a sharp water-air interface.

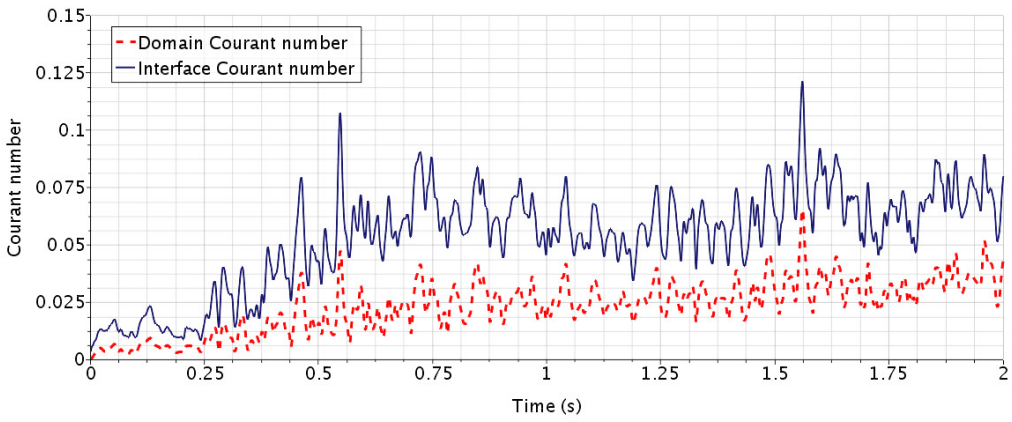

Figure 4.10: Volume averaged Courant number for the water-air interface and the entire domain. The average Courant number is always below 0.5.

4.2.2 FSI Analysis

In this section, the results from the FSI simulations on the Volvo tank (Figure 3.13) are discussed. The FSI methodology within STAR-CCM+, as described in subsection 3.1.2, is used for the *one-way* and *two-way* coupled FSI simulations. The results are compared with the experiments carried out at the testing facilities at Volvo.

Running transient FSI simulations for a period of 5 s for the *out-of-phase washboard* acceleration signal is computationally expensive and time consuming, despite using high performance computing through multiple parallel processors on a cluster. This is owing to the fact that the computational process involves solving two different domains communicating with each other at every time-step. An optimum number of processors is therefore required because too many processors increase the memory requirement for a correspondingly increased number of communications across the solid-fluid interface, thereby leading to poor scaling of the domain(s).

For a two-way coupled simulation, the computational expenses increase manyfold. This is due to two reasons — first, the fluid and solid domains are solved and the field variables are exchanged across the interface every inner iteration of a time step; second, the mesh morphing step, that takes place every inner iteration, can be handled only by one processor. Due to these reasons, the two-way coupled simulations are carried out on a coarser mesh with 1.36 million cells for 2 s of the acceleration signal and the results are compared with one-way coupled simulations (for the same mesh configuration).

4.2.2.1 One-Way Coupled Simulations

The one-way coupled FSI simulations are carried out on the final mesh configuration comprising of about 9 million cells in the fluid and solid domains together for the whole 5 s of the acceleration signal. For each fill level, it takes one week of computational time on 4 CPU's (Intel(R) Xeon(R) CPU E5-2680 v2 @ 2.80GHz) with 10 cores each.

Figure 4.11 shows the contours of pressure (on the fluid side) and Von-Mises stress (on the solid side) of the end plate at a few time instances. The contribution of wall-shear-stress to the traction supplied to the solid domain is negligible, and has therefore not been shown here. It is clear from the figure that high pressure regions correspond to high stress regions on the end plate.

The in-plane strain data obtained from the experimental setup, as described in section 3.2, is compared with the one-way coupled FSI simulations. Figures 4.12 - 4.15 show the comparison of strains for 20%, 40%, 60%, and 80% fill levels at a couple of strain gauge locations on the end walls of the tank ($Stg1$ and $Stg4$). It is clear that for all the fill levels in both strain gauge locations, the numerical simulations capture the essential trend of the strains from the experiments, i.e., high strain levels at the start of the acceleration signal, followed by diminishing strains in the later half.

The differences between the experimental and numerical results are quantified by looking at the peaks of the strains because it is the impact strains (and not the mean strains) that can cause the tank structure to fail. For this purpose, the *envelope* function of the MATLAB signal processing toolbox [45] was used to find the upper and lower bounds of the transient strain signals (see Figure 4.16). The percentage deviation of the average of the numerical *maximum* strains from the experiments is plotted in Figure 4.17 for different fill levels at the four strain gauge locations. It is interesting to note that for all strain gauges, the comparison of the numerical and experimental results is best for the 20% fill level and the accuracy decreases with increasing fill levels (except $Stg2$, for reasons yet unknown). This can be attributed to the fact that the sloshing loads on the tank increase with increasing fill levels and the inability of the one-way coupled method to accurately predict all the essential features. The comparisons of experimental and numerical strain data of $Stg2$ and $Stg3$ are included in Appendix A.

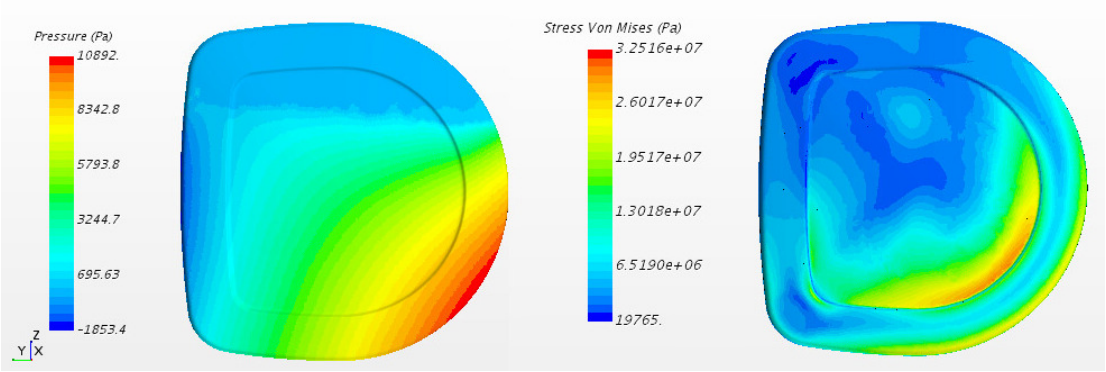

(a) $t = 2.5\ s$

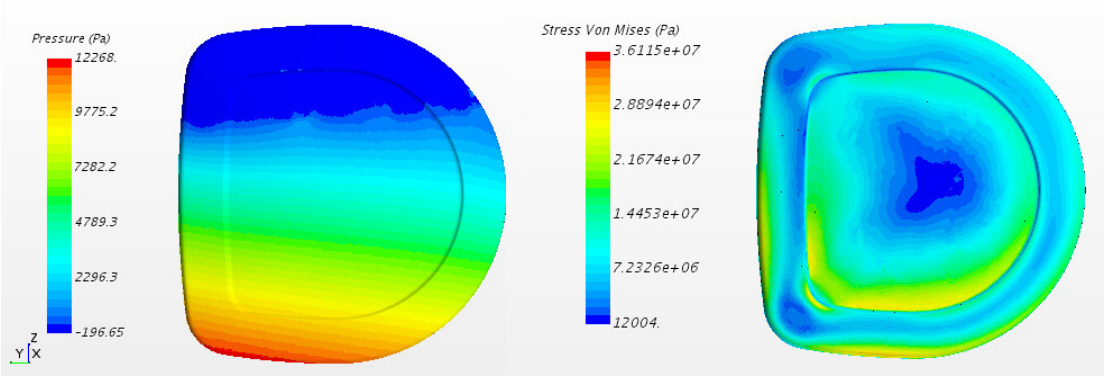

(b) $t = 3.5\ s$

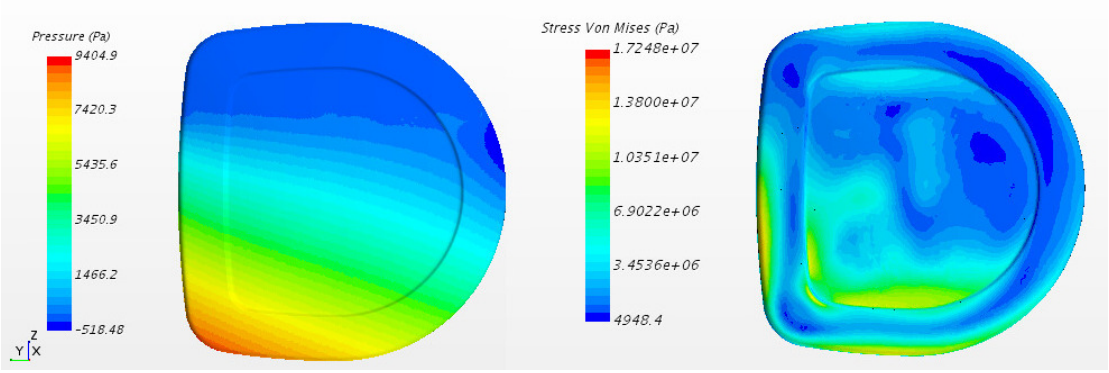

(c) $t = 4.375\ s$

Figure 4.11: Contours of pressure and Von Mises stress at some time instances on the tank end plate

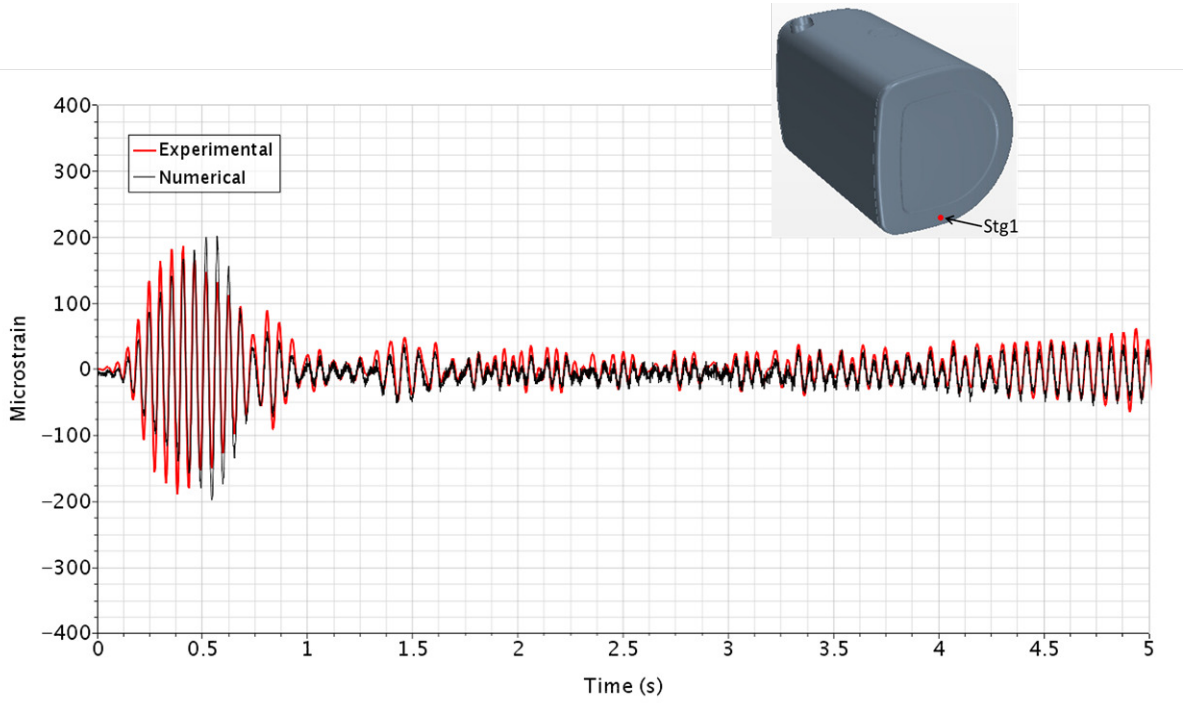

(a) 20% Filling

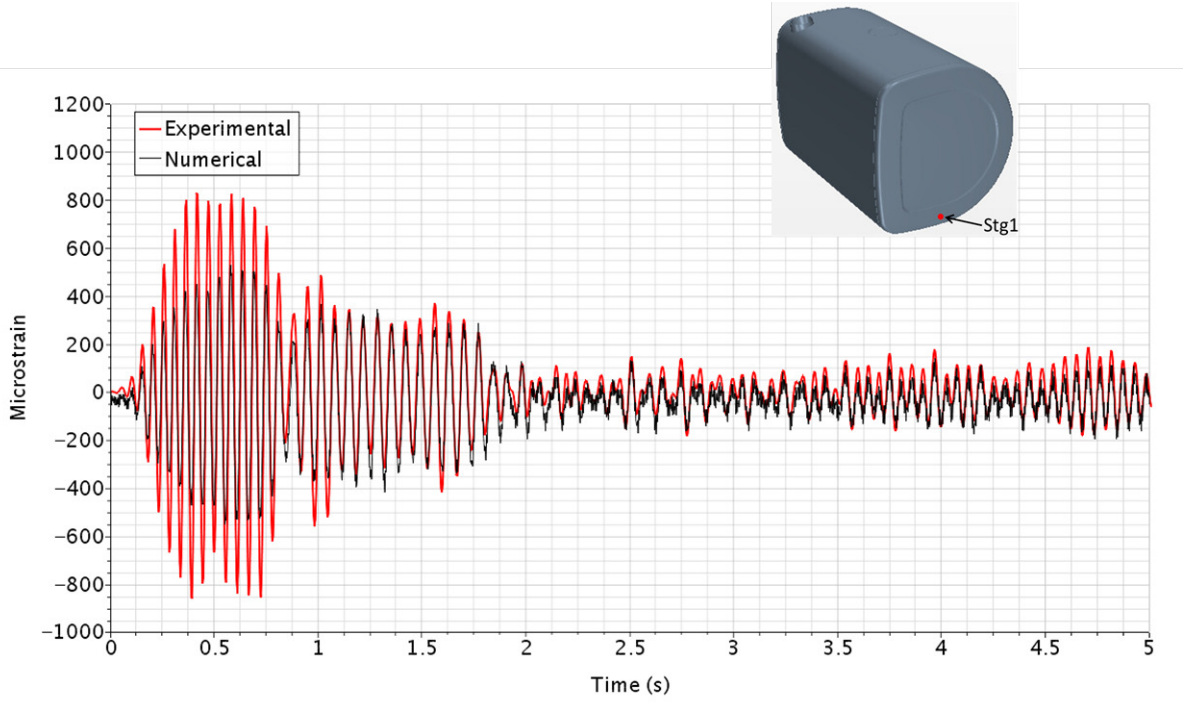

(b) 40% Filling

Figure 4.12: Comparison of strains obtained from *one-way coupled* simulations and experimental results at $Stg1$ for 20% and 40% fill levels

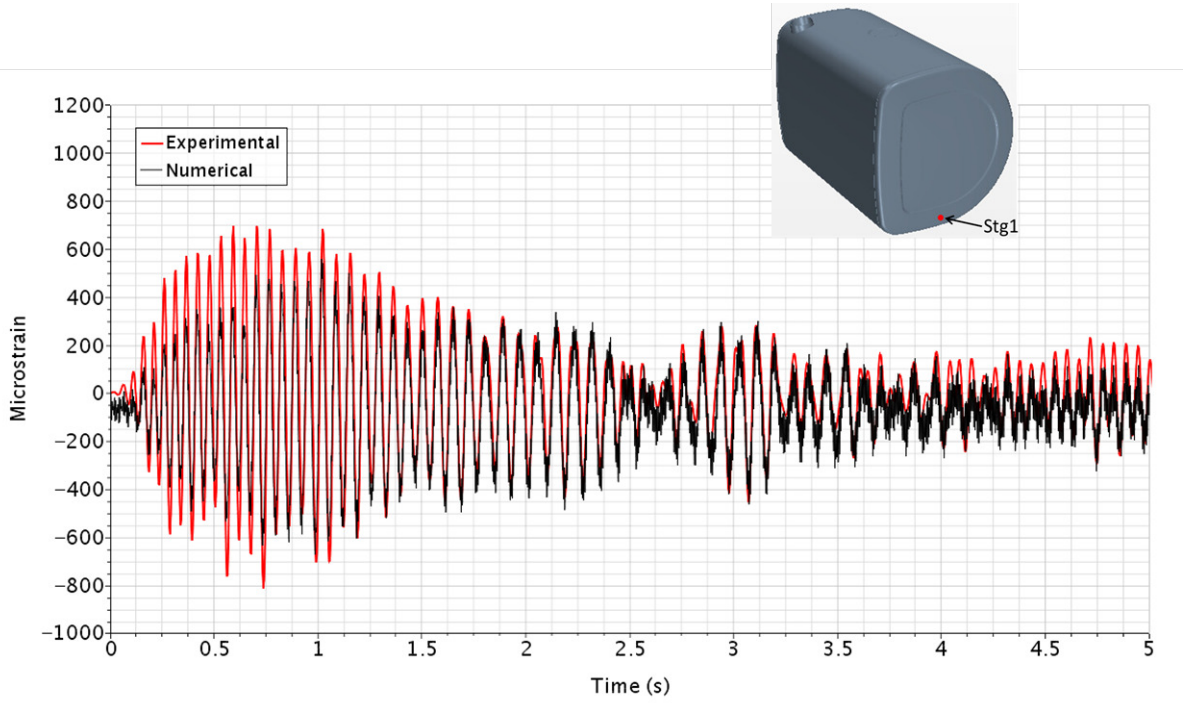

(a) 60% Filling

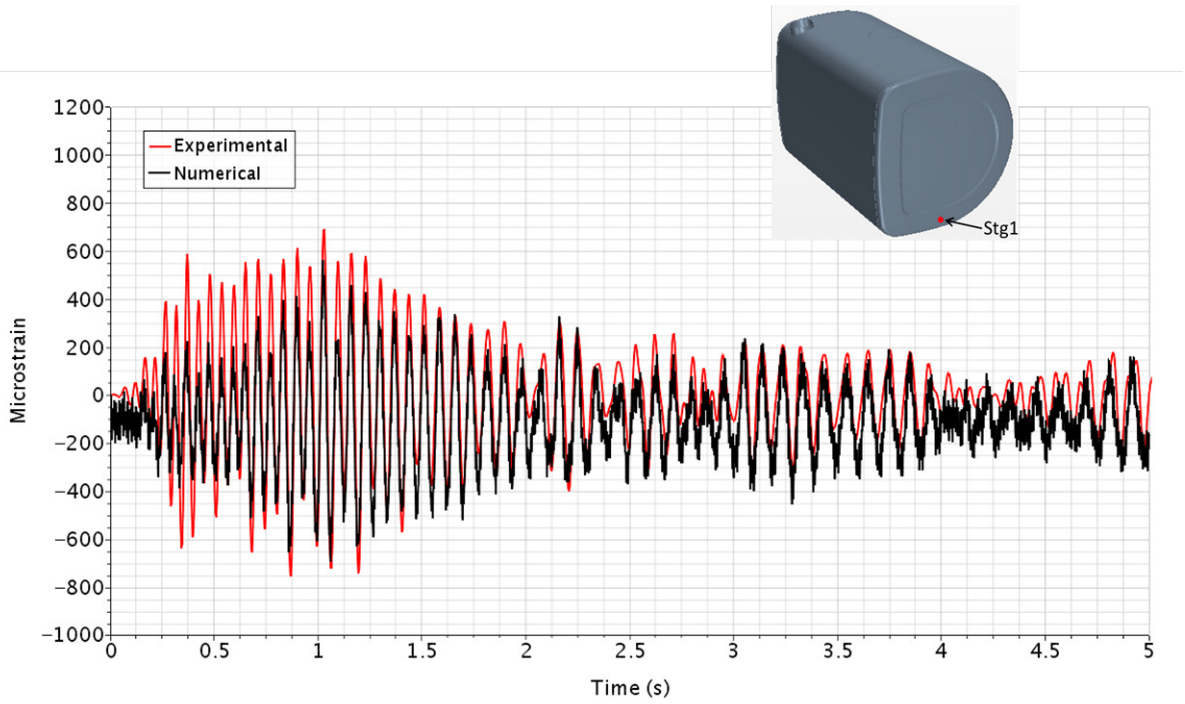

(b) 80% Filling

Figure 4.13: Comparison of strains obtained from *one-way coupled* simulations and experimental results at strain gauge $Stg1$ for 60% and 80% fill levels

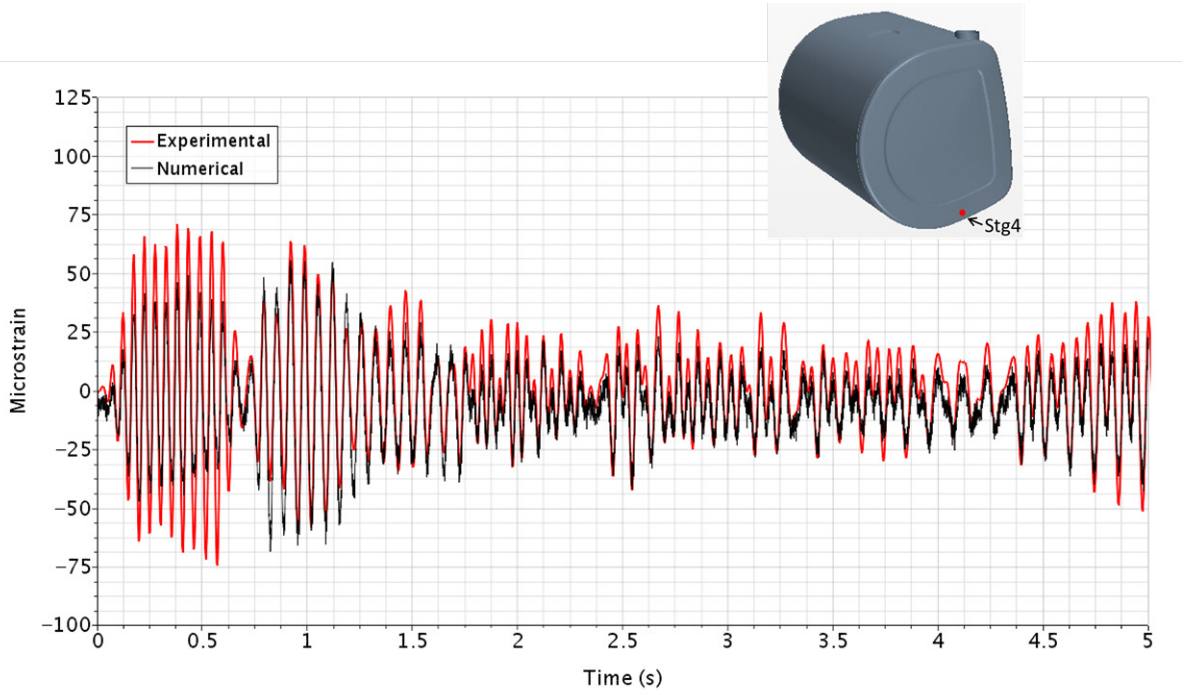

(a) 20% Filling

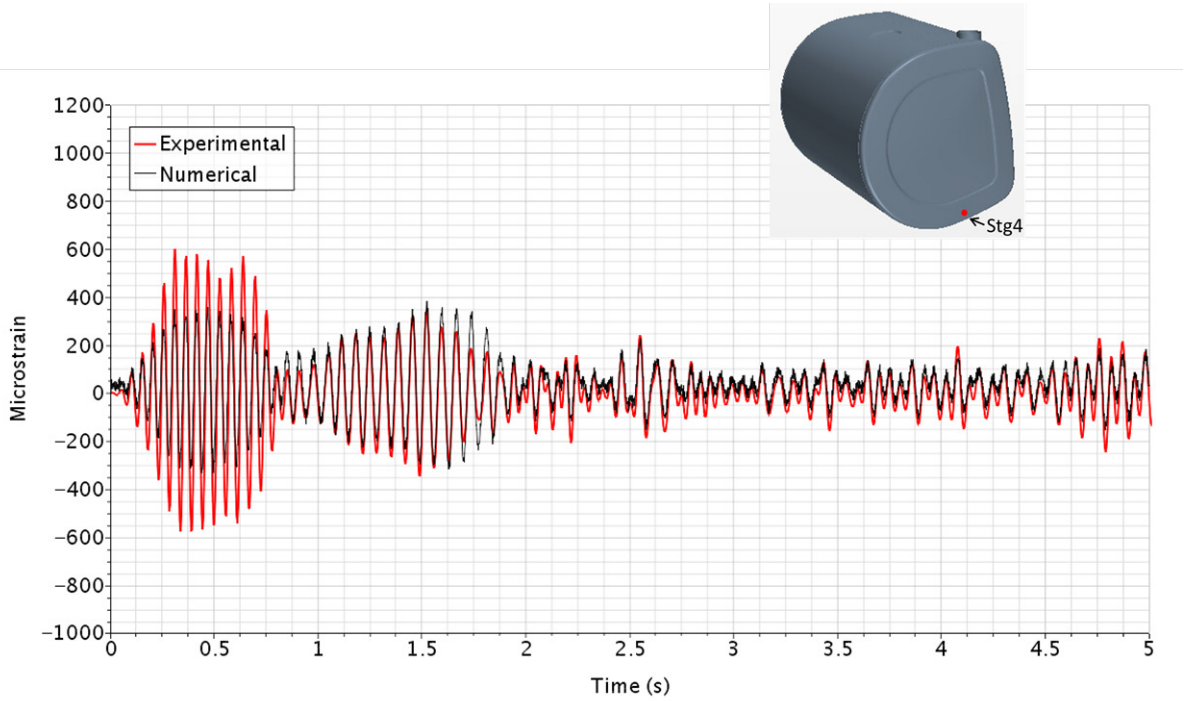

(b) 40% Filling

Figure 4.14: Comparison of strains obtained from *one-way coupled* simulations and experimental results at strain gauge *Stg*4 for 20% and 40% fill levels

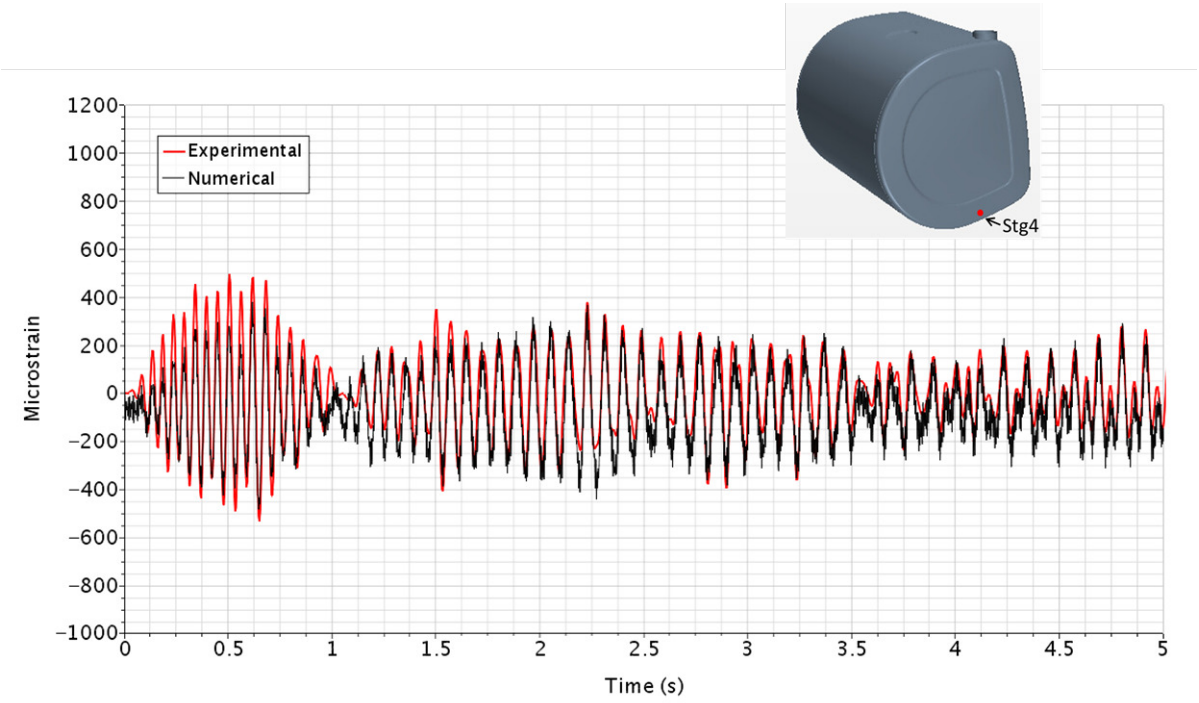

(a) 60% Filling

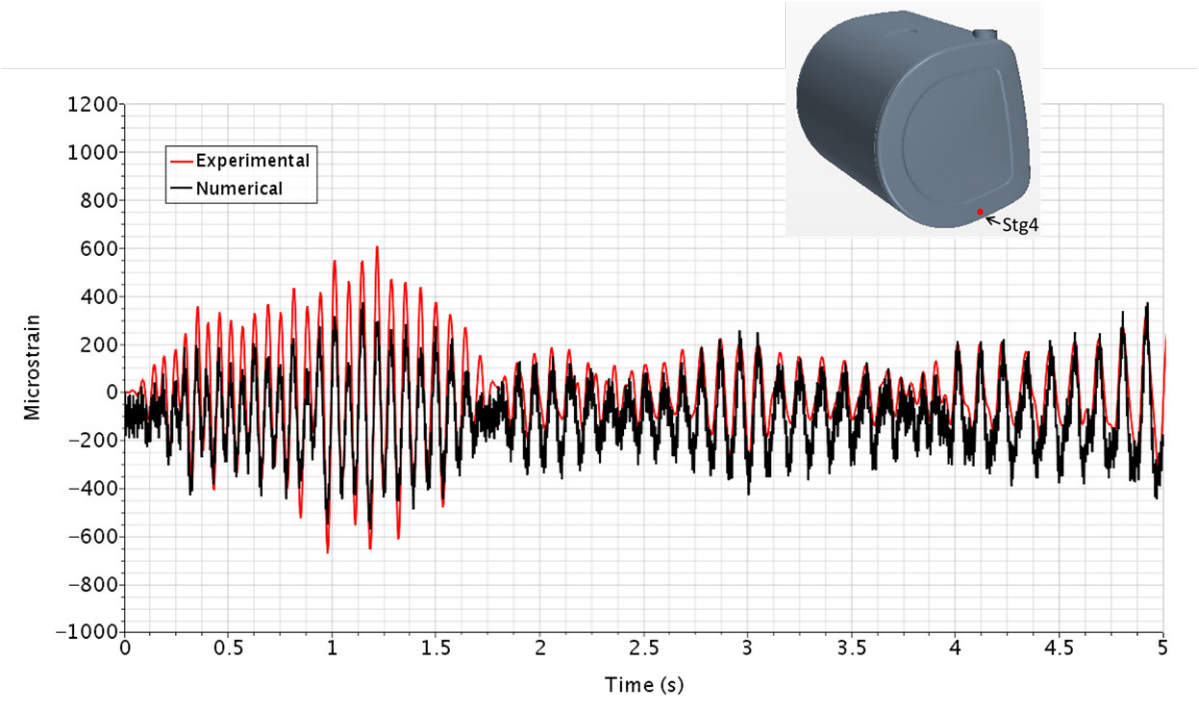

(b) 80% Filling

Figure 4.15: Comparison of strains obtained from *one-way coupled* simulations and experimental results at strain gauge *Stg*4 for 60% and 80% fill levels

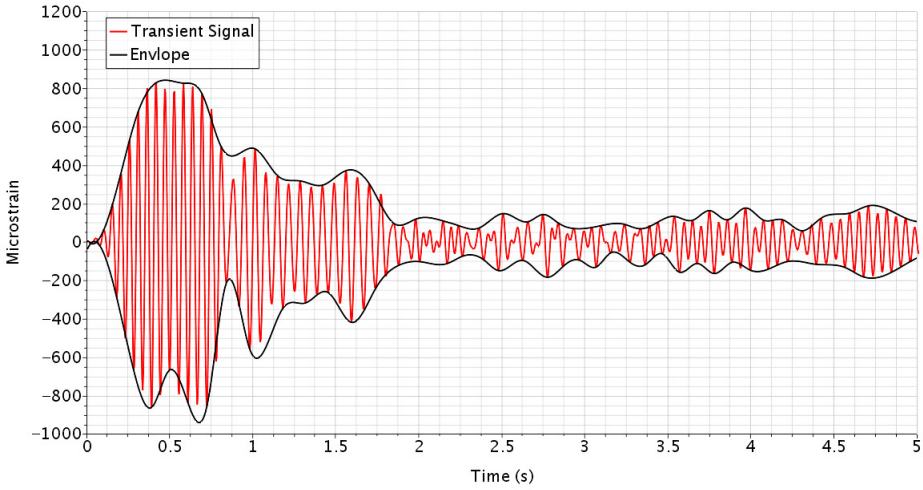

(a) Experimental strain envelopes

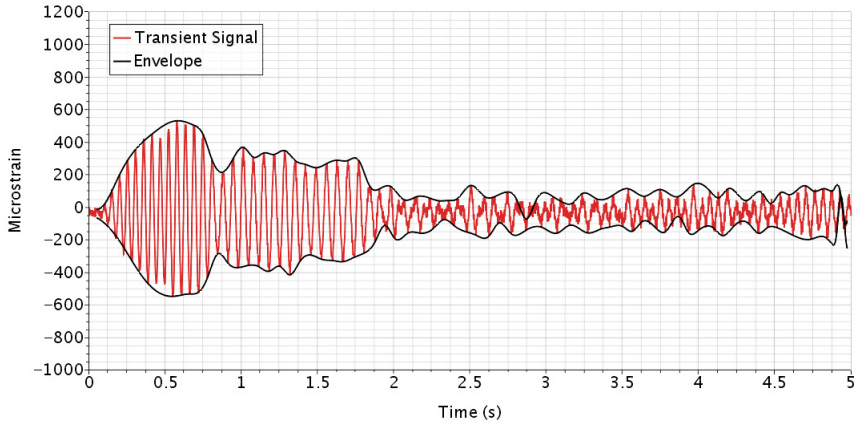

(b) Numerical strain envelopes

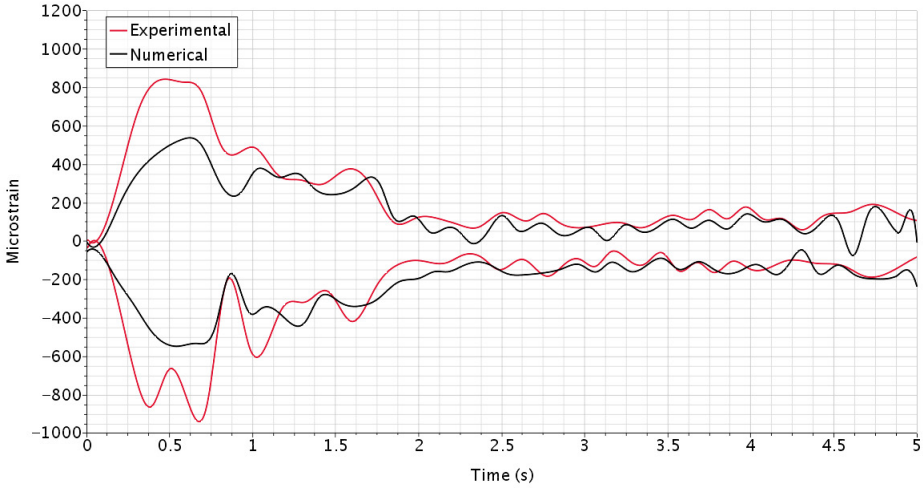

(c) Comparison of experimental and numerical strain envelopes

Figure 4.16: Envelopes for transient strain signals for 40% filling at strain gauge $Stg1$

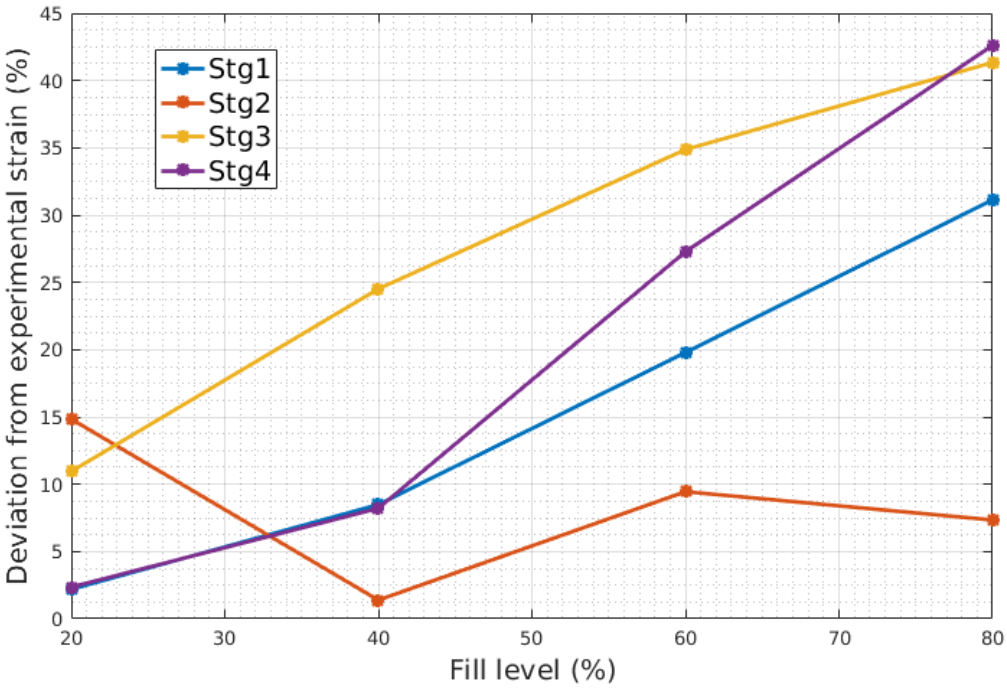

Figure 4.17: Deviation of the *one-way coupled* simulations from experimental results. Note the increase in deviation from experiments with increasing fill levels.

4.2.2.2 Two-Way Coupled Simulations

As mentioned before, the two-way coupled simulations were performed only for the first 2 s of the acceleration signal on the coarse mesh with 1.36 million cells. Also, high loads on the solid domain due to high fill levels (60% and 80%) rendered the simulations very unstable. First-order temporal discretization, under-relaxation factors, and increased inner-iterations in a time step were used to circumvent issues of instability in the numerics. This, however, further increased the computational costs and therefore due to time constraints, simulations were carried out for 20% and 40% fill levels only.

From Figures 4.18 and 4.19, it is clear that for 20% fill level, the one-way and two-way coupled simulations yield nearly the same strain levels. For 40% fill level, the two-way coupled simulations are able to capture the high sloshing-induced strains better than the one-way coupled simulations for the same mesh configuration, resulting in close comparison with the experimental signals. However, this comes at very high costs — the computational time for running a two-way coupled simulation was around ten times more than a one-way coupled simulation.

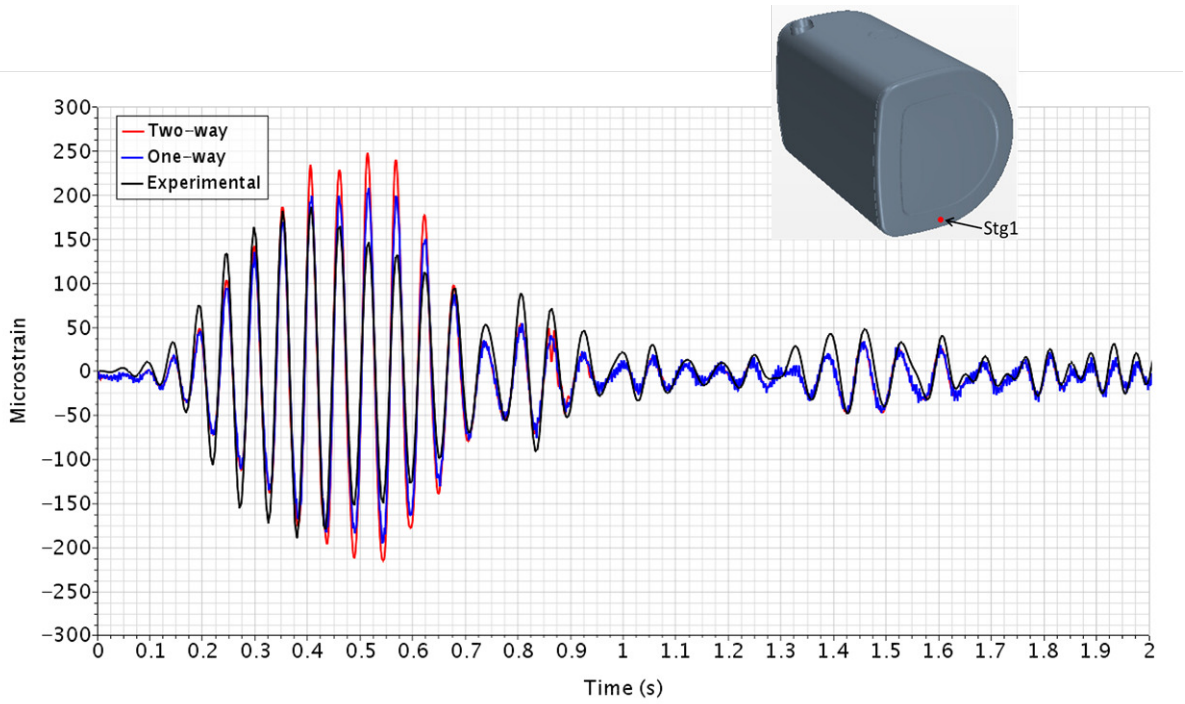

(a) 20% Filling

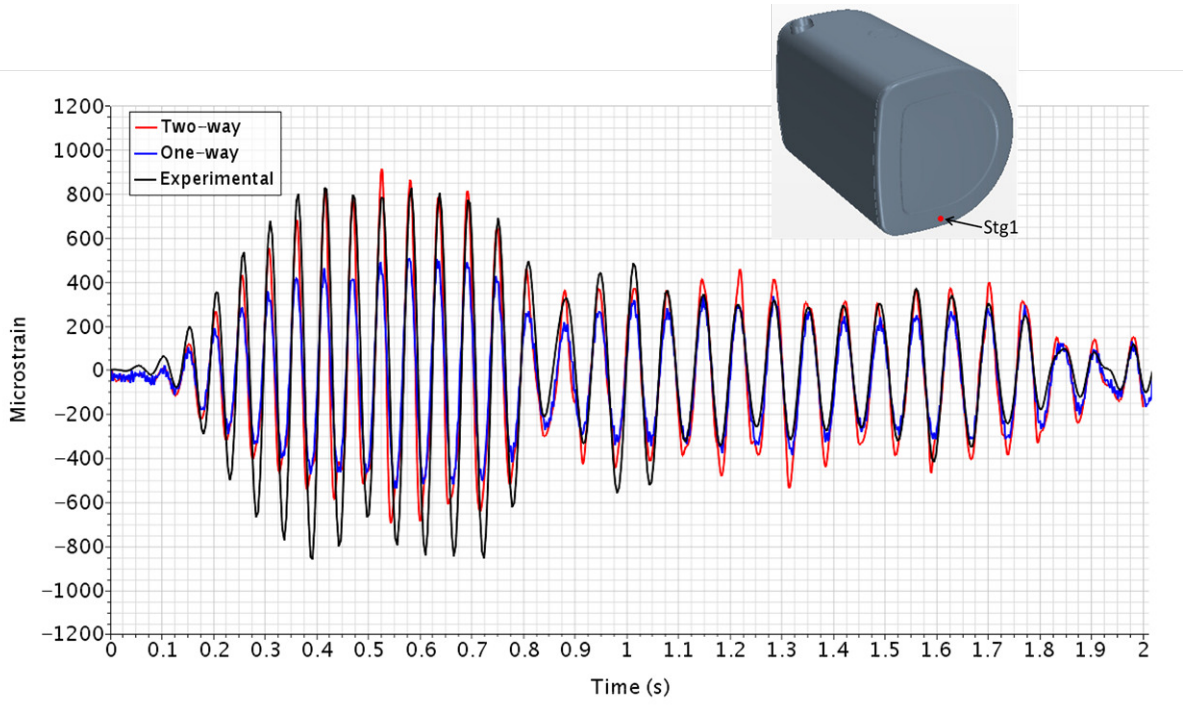

(b) 40% Filling

Figure 4.18: Comparison of strains obtained from *one-way* and *two-way coupled* simulations with experimental results at strain gauge *Stg*1 for 20% and 40% fill levels

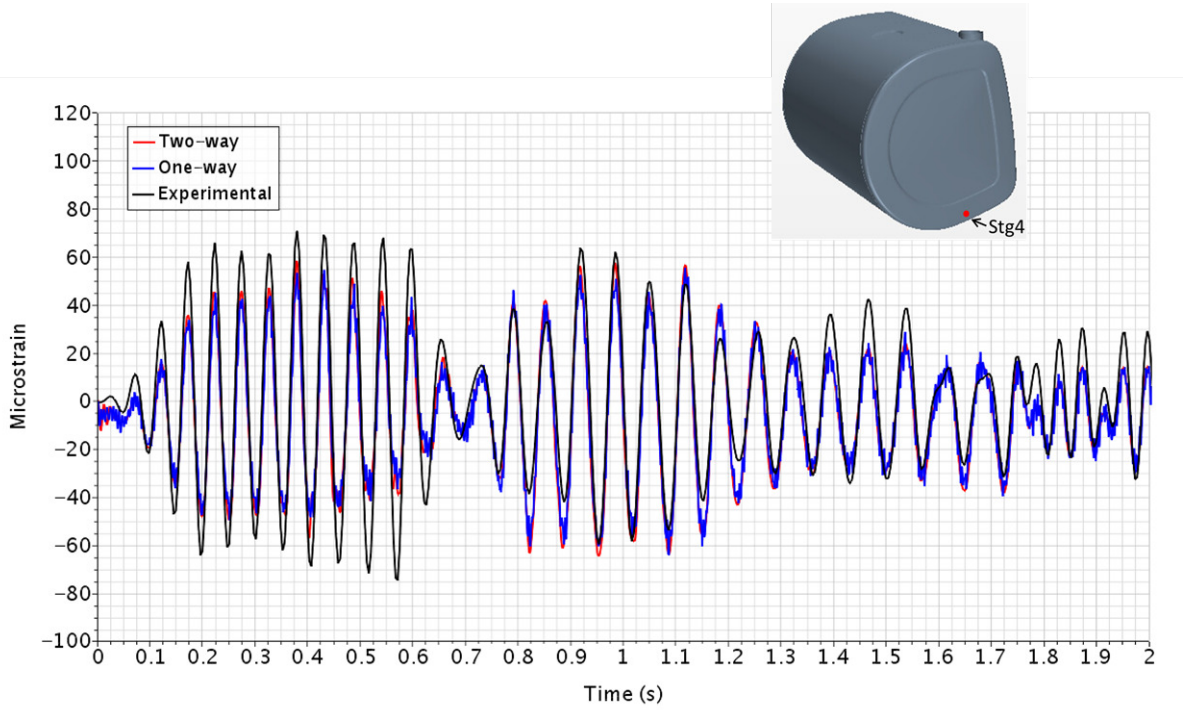

(a) 20% Filling

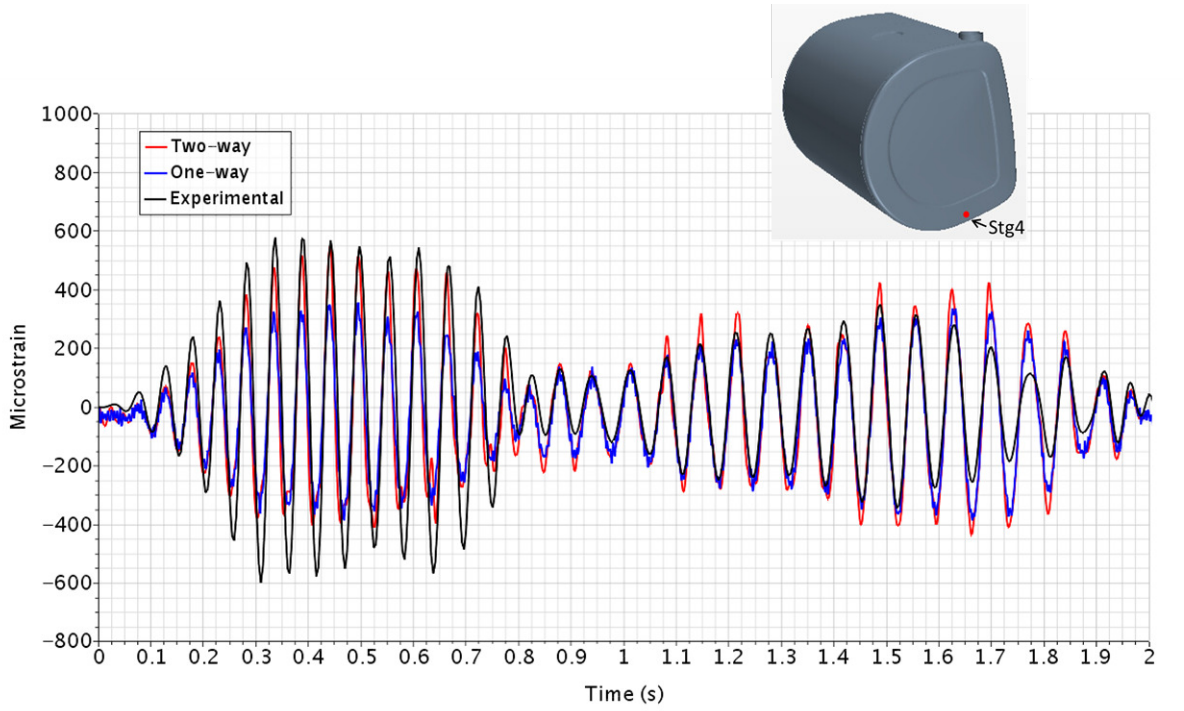

(b) 40% Filling

Figure 4.19: Comparison of strains obtained from *one-way* and *two-way coupled* simulations with experimental results at strain gauge *Stg*4 for 20% and 40% fill levels

5
Conclusion

Analysis of sloshing-induced loads on the fuel tank structure is carried out using the partitioned FSI approach. Validations of the VOF and the coupled CFD-FEA methodologies with numerical and experimental results from the literature on simplified representative tank geometries lay the foundation for the analysis of the Volvo fuel tank. Low-frequency and high amplitude acceleration signals from the test track, corresponding to the worst case scenario for sloshing are considered for the analyses.

A fair comparison of the one-way coupled FSI simulations with experiments conducted at Volvo is obtained. It is seen that the deviations from the experimental results increase with increasing fill levels, attributed to the increased loads and the resulting structural displacements that are not accurately captured in the one-way coupled simulations. This is further reinforced by the results from the two-way coupled simulations that compare well with the physical tests. The two-way coupled simulations are, however, highly computationally expensive and can often be impractical for running simulations on the industrial scale for long-duration acceleration signals.

Close comparison of the FSI results obtained by coupling Abaqus with STAR-CCM+ and the ones by using the STAR-CCM+ framework only (subsection 3.1.2) motivated the use of STAR-CCM+ for the final analysis. Experimental verification of this method stands as evidence of the credibility of the FSI handling capabilities of STAR-CCM+. This approach is advantageous in that there are less license-related constraints and complexities involved in coupling two separate solvers.

Simulations on a simplified tank with similar geometric features as the Volvo fuel tank show increasing trends of wall-impact pressures and displacements with increasing fill levels. Interestingly, a decrease in the displacements at the baffle was observed owing to the presence of the holes at nearly the same level as the liquid free surface for the highest fill level. A similar phenomenon might be observed for other fill levels, hole locations and hole diameters. Thus, the simulation methodology developed in this work can also be used in the geometrical optimization of the fuel tank to reduce the impacts of sloshing.

A comparative analysis of the two-way coupled simulations with experiments for 60% and 80% filling levels needs to be made in the future simulations. Since cracks were observed on the baffles and end plates for excessively loaded tanks over a number of load cycles during test runs, it is evident that the failure is associated

with fatigue. The simulation methodology developed in this work does not include effects of fatigue loads and a further investigation is therefore necessary to make a comprehensive structural analysis of the fuel tanks. Also, the effects of including fuel instead of water as liquid phase need to be analyzed in the future simulations. Due to time constraints, effects of increasing or reducing the solid mesh resolution have not been analyzed. This could also form a part of the future work.

Bibliography

[1] Eswaran, M., Saha, U.K. and Maity, D., 2009. Effect of baffles on a partially filled cubic tank: Numerical simulation and experimental validation. Computers & Structures, 87(3), pp.198-205.

[2] Sankar, S., Ranganathan, R. and Rakheja, S., 1992. Impact of dynamic fluid slosh loads on the directional response of tank vehicles. Vehicle System Dynamics, 21(1), pp.385-404.

[3] Fischer, F.D. and Rammerstorfer, F.G., 1999. A refined analysis of sloshing effects in seismically excited tanks. International Journal of Pressure Vessels and Piping, 76(10), pp.693-709.

[4] Nicolici, S. and Bilegan, R.M., 2013. Fluid structure interaction modeling of liquid sloshing phenomena in flexible tanks. Nuclear Engineering and Design, 258, pp.51-56.

[5] Zhou, W., Wu, Z. and Mevel, L., 2010. Vibration-based damage detection to the composite tank filled with fluid. Structural Health Monitoring, 9(5), pp.433-445.

[6] Kamiya, K., Yamaguchi, Y. and De Vries, E., 2002. Simulation studies of sloshing in a fuel tank (No. 2002-01-0574). SAE Technical Paper.

[7] Myrillas, K., Planquart, P., Buchlin, J.M. and Schyns, M., 2016. Small scale experiments of sloshing considering the seismic safety of MYRRHA. International Journal of Hydrogen Energy, 41(17), pp.7239-7251.

[8] Jung, J.H., Yoon, H.S. and Lee, C.Y., 2015. Effect of natural frequency modes on sloshing phenomenon in a rectangular tank. International Journal of Naval Architecture and Ocean Engineering, 7(3), pp.580-594.

[9] Wachowski, C., Biermann, J.W. and Schala, R., 2010, September. Approaches to analyse and predict slosh noise of vehicle fuel tanks. In 24th International Conference of Noise and Vibration Engineering (ISMA2010), Belgium.

[10] Vaishnav, D., Dong, M., Shah, M., Gomez, F. and Usman, M., 2014. Investigation and Development of Fuel Slosh CAE Methodologies. SAE International Journal of Passenger Cars-Mechanical Systems, 7(2014-01-1632), pp.278-288.

[11] Akyildiz, H. and Ünal, E., 2005. Experimental investigation of pressure distribution on a rectangular tank due to the liquid sloshing. Ocean Engineering, 32(11), pp.1503-1516.

[12] Liu, D. and Lin, P., 2009. Three-dimensional liquid sloshing in a tank with baffles. Ocean engineering, 36(2), pp.202-212.

[13] Panigrahy, P.K., Saha, U.K. and Maity, D., 2009. Experimental studies on sloshing behavior due to horizontal movement of liquids in baffled tanks. Ocean Engineering, 36(3), pp.213-222.

[14] Jung, J.H., Yoon, H.S., Lee, C.Y. and Shin, S.C., 2012. Effect of the vertical baffle height on the liquid sloshing in a three-dimensional rectangular tank. Ocean Engineering, 44, pp.79-89.

[15] Paik, K.J. and Carrica, P.M., 2014. Fluid–structure interaction for an elastic structure interacting with free surface in a rolling tank. Ocean Engineering, 84, pp.201-212.

[16] Hwang, S.C., Park, J.C., Gotoh, H., Khayyer, A. and Kang, K.J., 2016. Numerical simulations of sloshing flows with elastic baffles by using a particle-based fluid–structure interaction analysis method. Ocean Engineering, 118, pp.227-241.

[17] Souto-Iglesias, A., Delorme, L., Pérez-Rojas, L. and Abril-Pérez, S., 2006. Liquid moment amplitude assessment in sloshing type problems with smooth particle hydrodynamics. Ocean Engineering, 33(11), pp.1462-1484.

[18] Shao, J.R., Li, H.Q., Liu, G.R. and Liu, M.B., 2012. An improved SPH method for modeling liquid sloshing dynamics. Computers & Structures, 100, pp.18-26.

[19] Field, Kristopher S., 2014, Liquid Slosh Analysis Using Smoothed Particle Hydrodynamics. Dissertations and Theses. Paper 159.

[20] Violeau, D. and Rogers, B.D., 2016. Smoothed particle hydrodynamics (SPH) for free-surface flows: past, present and future. Journal of Hydraulic Research, 54(1), pp.1-26.

[21] Weaver, T. and Xiao, Z., 2016, February. Fluid Simulation by the Smoothed Particle Hydrodynamics Method: A Survey. VISIGRAPP 2016-Proceedings of the 11th Joint Conference on Computer Vision, Imaging and Computer Graphics Theory and Applications 2016.

[22] Akyildız, H. and Ünal, N.E., 2006. Sloshing in a three-dimensional rectangular tank: numerical simulation and experimental validation. Ocean Engineering, 33(16), pp.2135-2149.

[23] Klostermann, J., Schaake, K. and Schwarze, R., 2013. Numerical simulation of a single rising bubble by VOF with surface compression. International Journal for Numerical Methods in Fluids, 71(8), pp.960-982.

[24] Osher, S. and Sethian, J.A., 1988. Fronts propagating with curvature-dependent speed: algorithms based on Hamilton-Jacobi formulations. Journal of computational physics, 79(1), pp.12-49.

[25] Hirt, C.W. and Nichols, B.D., 1981. Volume of fluid (VOF) method for the dynamics of free boundaries. Journal of computational physics, 39(1), pp.201-225.

[26] Nichita, B.A., Zun, I. and Thome, J.R., 2010. A Level Set Method Coupled With a Volume of Fluid Method for Modeling of Gas-Liquid Interface in Bubbly Flow. Journal of fluids engineering, 132(8), p.081302.

[27] Wang, Z., Yang, J., Koo, B. and Stern, F., 2009. A coupled level set and volume-of-fluid method for sharp interface simulation of plunging breaking waves. International Journal of Multiphase Flow, 35(3), pp.227-246.

[28] Godderidge, B., Turnock, S., Tan, M. and Earl, C., 2009. An investigation of multiphase CFD modelling of a lateral sloshing tank. Computers & Fluids, 38(2), pp.183-193.

[29] Rhee, S.H., 2005. Unstructured grid based Reynolds-averaged Navier-Stokes method for liquid tank sloshing. Journal of fluids engineering, 127(3), pp.572-582.

[30] Tezdogan, T., Demirel, Y.K., Kellett, P., Khorasanchi, M., Incecik, A. and Turan, O., 2015. Full-scale unsteady RANS CFD simulations of ship behaviour and performance in head seas due to slow steaming. *Ocean Engineering, 97*, pp.186-206.

[31] Gao, Z., Vassalos, D. and Gao, Q., 2010. Numerical simulation of water flooding into a damaged vessel's compartment by the volume of fluid method. Ocean Engineering, 37(16), pp.1428-1442.

[32] Shih, T.H., Liou, W.W., Shabbir, A., Yang, Z. and Zhu, J., 1995. A new $k-\epsilon$ eddy viscosity model for high reynolds number turbulent flows. Computers & Fluids, 24(3), pp.227-238.

[33] CD-adapco. *STAR-CCM+ Version 11.06 User Guide*, 2016.

[34] Hron, J. and Turek, S. A Monolithic FEM Solver for ALE Formulation of Fluid Structure Interaction with Configurations for Numerical Benchmarking. In *Computational Methods for Coupled Problems in Science and Engineering* (1st edn), M. Papadrakakis, E. Onate, and B. Schrefler, editors, International Center for Numerical Methods in Engineering: Barcelona, 2005; 148. Konferenzband *'First International Conference on Computational Methods for Coupled Problems in Science and Engineering'*, Santorini, 25–27 May 2005.

[35] Wick, T. Solving monolithic fluid-structure interaction problems in arbitrary Lagrangian Eulerian coordinates with the deal. ii library. Archive of Numerical Software, 1 (2013), pp. 1–19.

[36] Wall, W.A., Genkinger, S. and Ramm, E., 2007. A strong coupling partitioned approach for fluid–structure interaction with free surfaces. Computers & Fluids, 36(1), pp.169-183.

[37] Causin, P., Gerbeau, J.F. and Nobile, F., 2005. Added-mass effect in the design of partitioned algorithms for fluid–structure problems. Computer methods in applied mechanics and engineering, 194(42), pp.4506-4527.

[38] Gatzhammer, B. (2008). A Partitioned Approach for Fluid-Structure Interaction on Cartesian Grids. Master's thesis, Technische Universitaet Muenchen.

[39] Hou, G., Wang, J. and Layton, A., 2012. Numerical methods for fluid-structure interaction—a review. Communications in Computational Physics, 12(2), pp.337-377.

[40] Degroote, J., 2013. Partitioned simulation of fluid-structure interaction. Archives of Computational Methods in Engineering, 20(3), pp.185-238.

[41] Quaini, A., 2009. Algorithms for fluid-structure interaction problems arising in hemodynamics. PhD thesis, Ecole Polytechnique Federale de Lausanne, Switzerland, 2008.

[42] Kim, Y., 2001. Numerical simulation of sloshing flows with impact load. Applied Ocean Research, 23(1), pp.53-62.

[43] Hsiao, S.C. and Lin, T.C., 2010. Tsunami-like solitary waves impinging and overtopping an impermeable seawall: Experiment and RANS modeling. Coastal Engineering, 57(1), pp.1-18.

[44] Idelsohn, S.R., Marti, J., Souto-Iglesias, A. and Onate, E., 2008. Interaction between an elastic structure and free-surface flows: experimental versus numerical comparisons using the PFEM. Computational Mechanics, 43(1), pp.125-132.
[45] The MathWorks, Inc., 2017. Signal Processing Toolbox User's Guide (R2017a).

A

Appendix 1

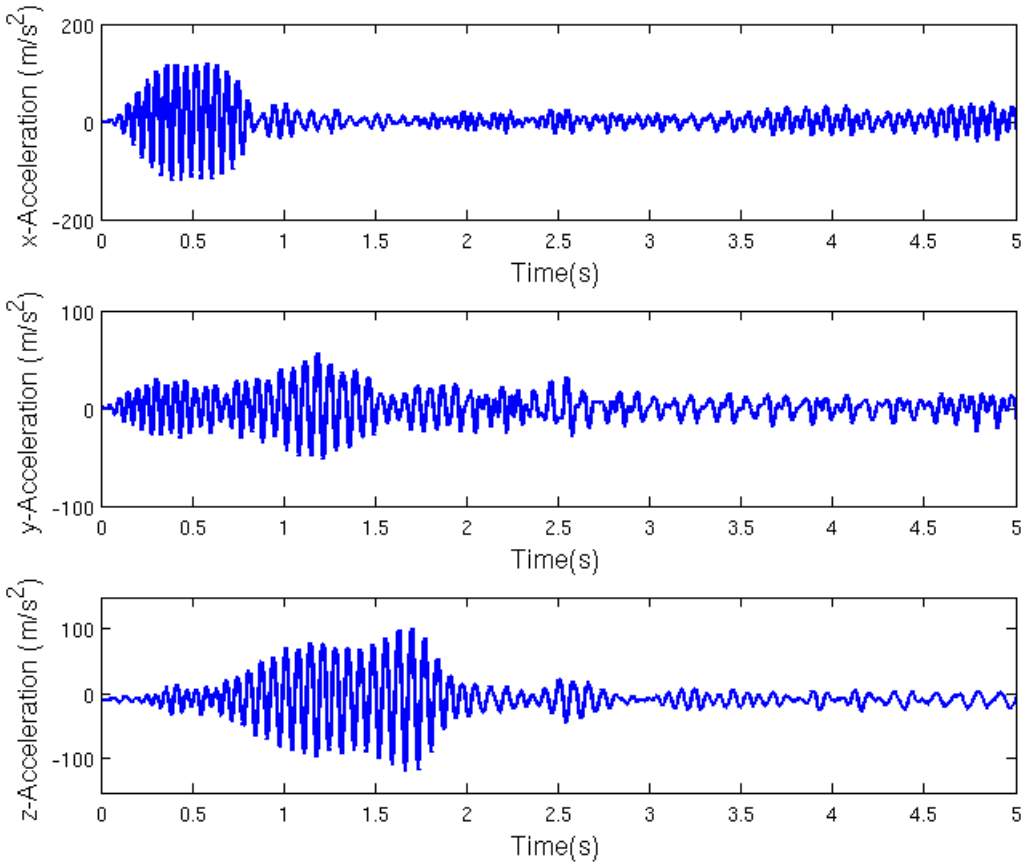

Figure A.1: Input acceleration signal corresponding to the out-of-phase washboard obstacle for a 40% filled tank

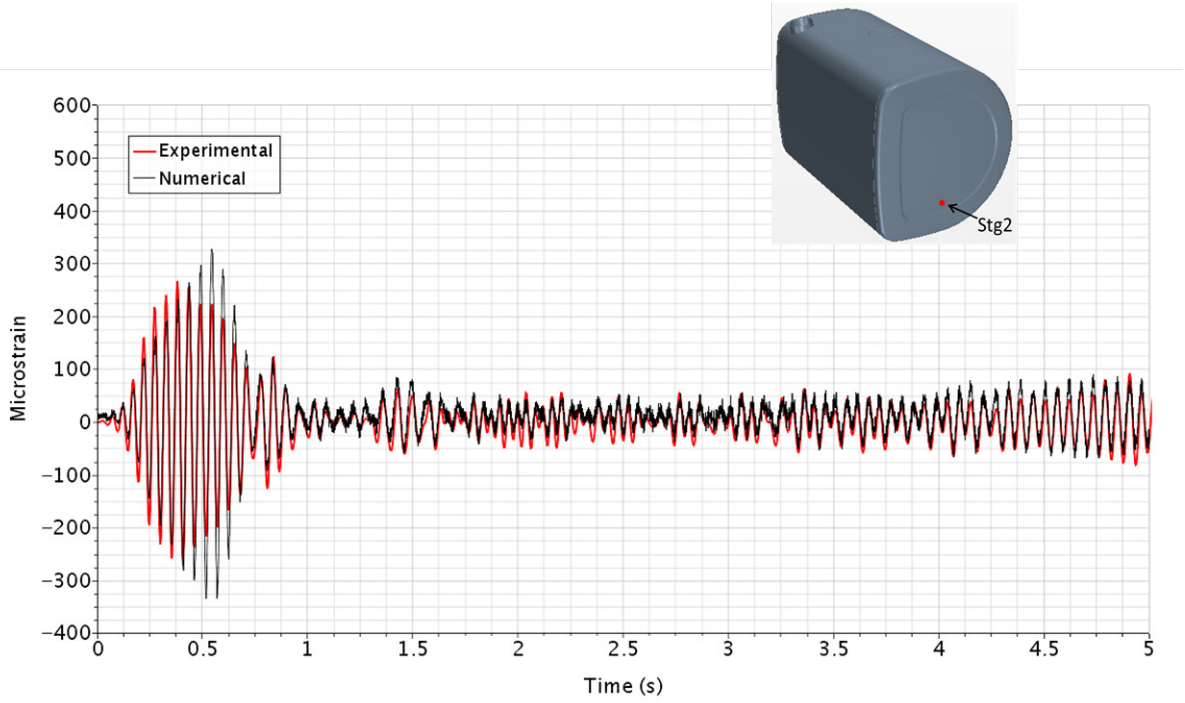

(a) 20% Filling

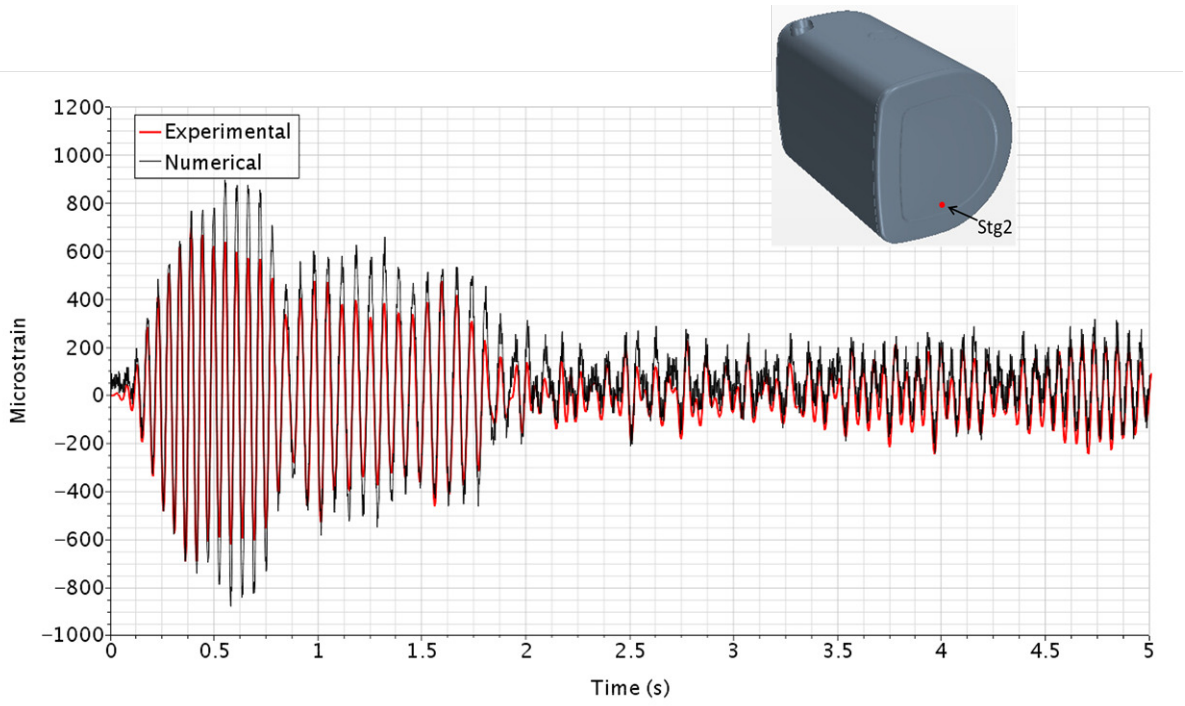

(b) 40% Filling

Figure A.2: Comparison of strains obtained from *one-way coupled* simulations and experimental results at strain gauge *Stg*2 for 20% and 40% fill levels

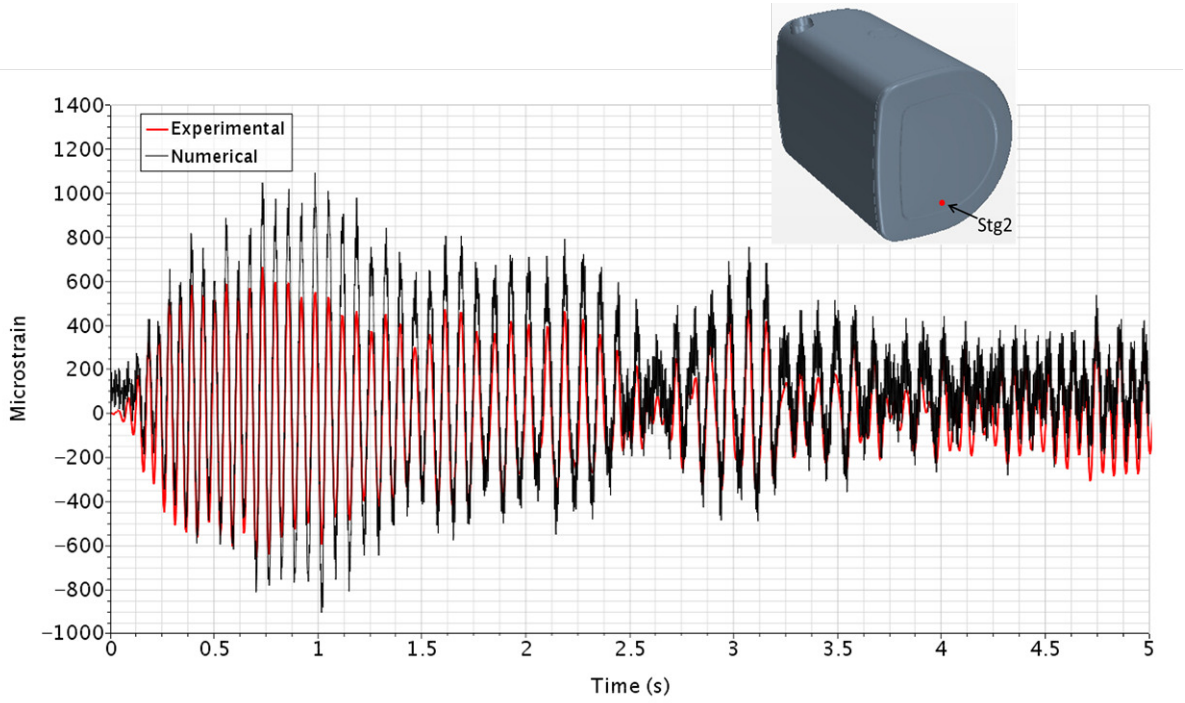

(a) 60% Filling

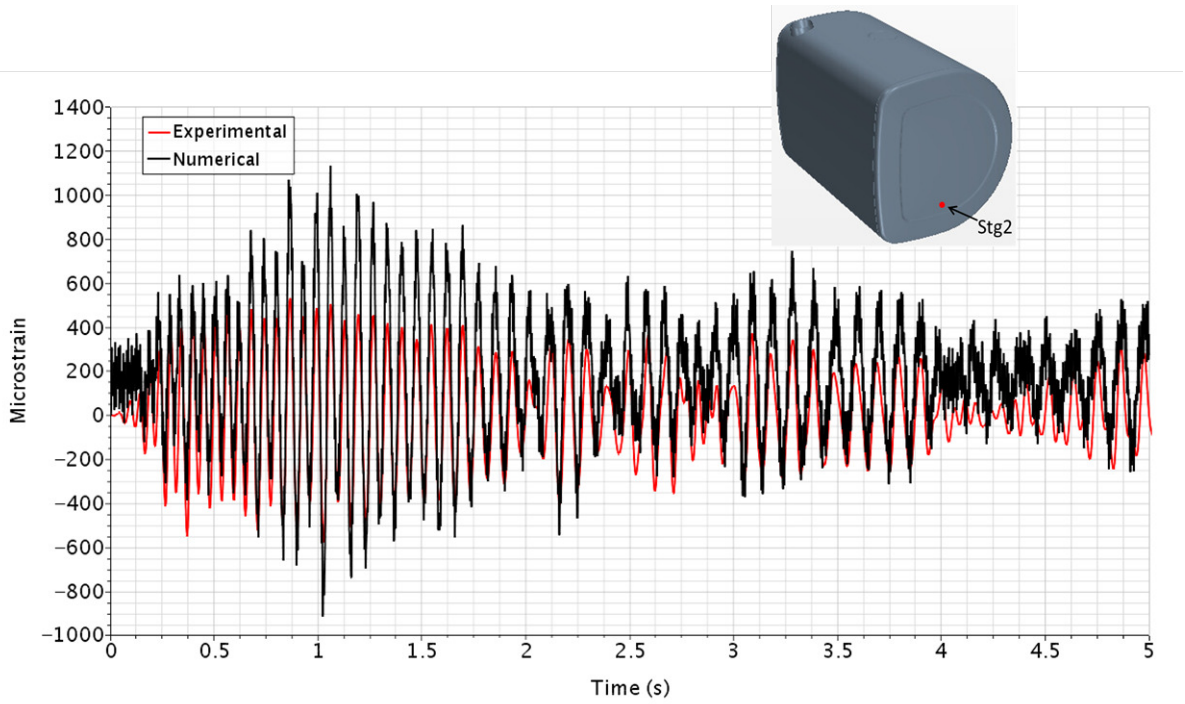

(b) 80% Filling

Figure A.3: Comparison of strains obtained from *one-way coupled* simulations and experimental results at strain gauge *Stg*2 for 60% and 80% fill levels

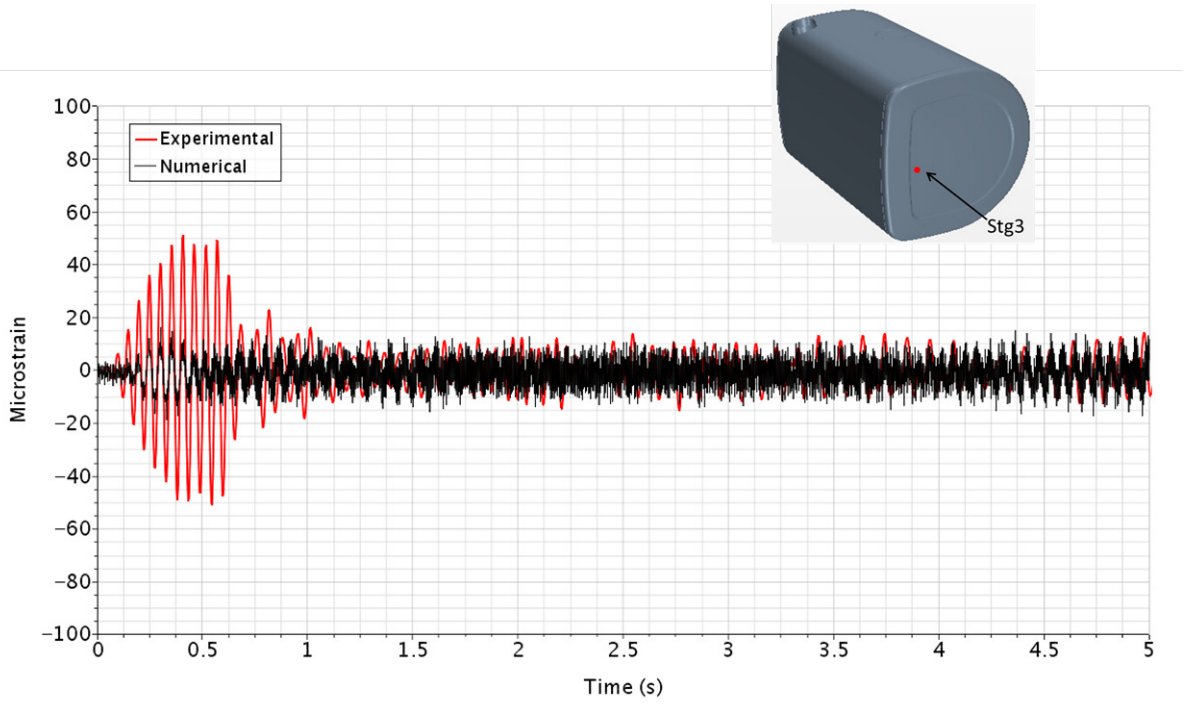

(a) 20% Filling

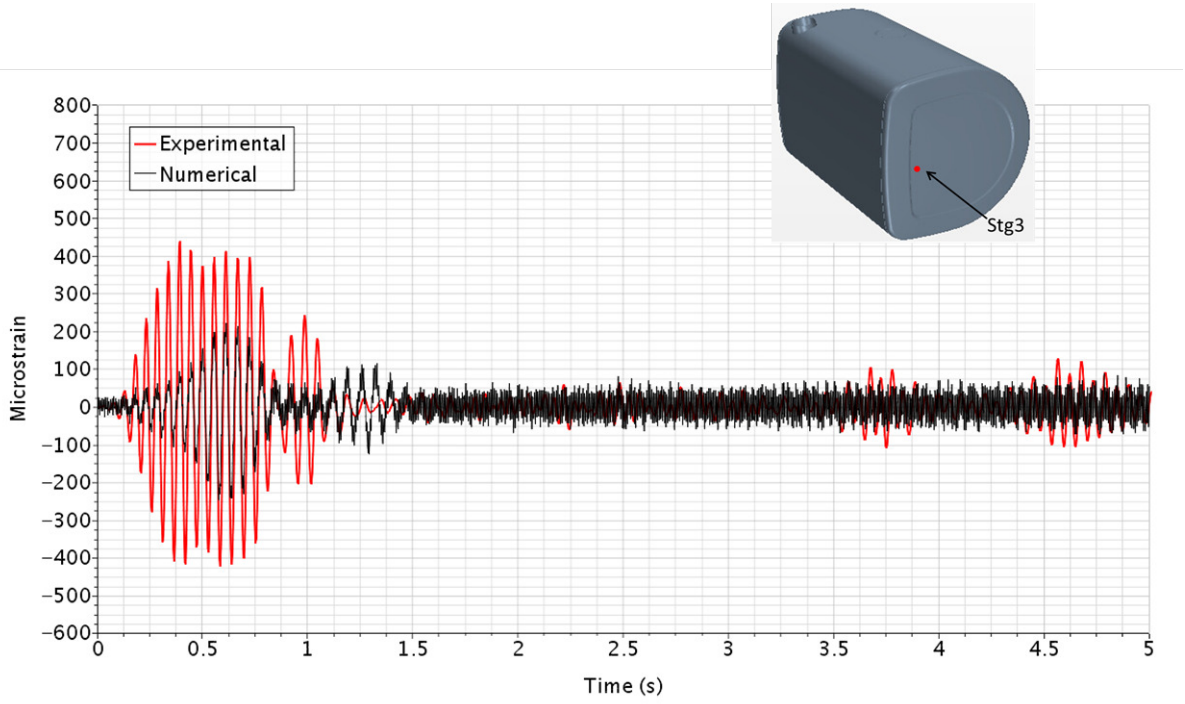

(b) 40% Filling

Figure A.4: Comparison of strains obtained from *one-way coupled* simulations and experimental results at *Stg*3 for 60% and 80% fill levels.
It is to be noted that the location of this strain gauge is well above the free surface for these fill levels and therefore the deviation from the experimental results are large.

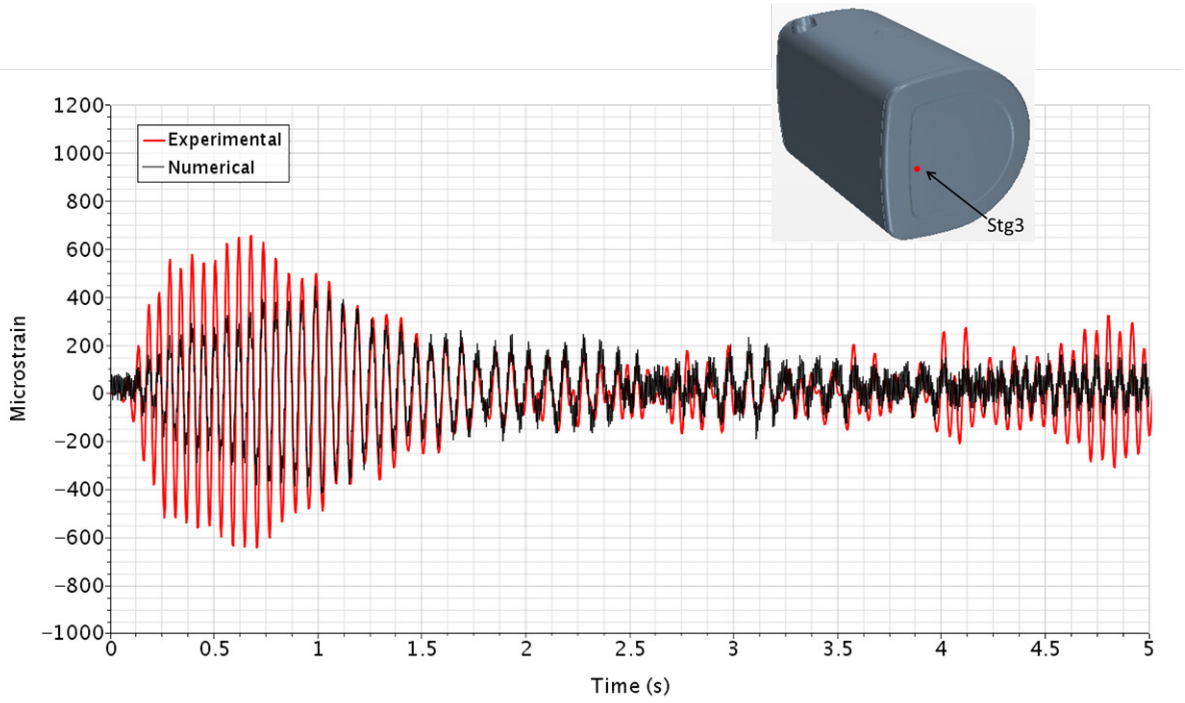

(a) 60% Filling

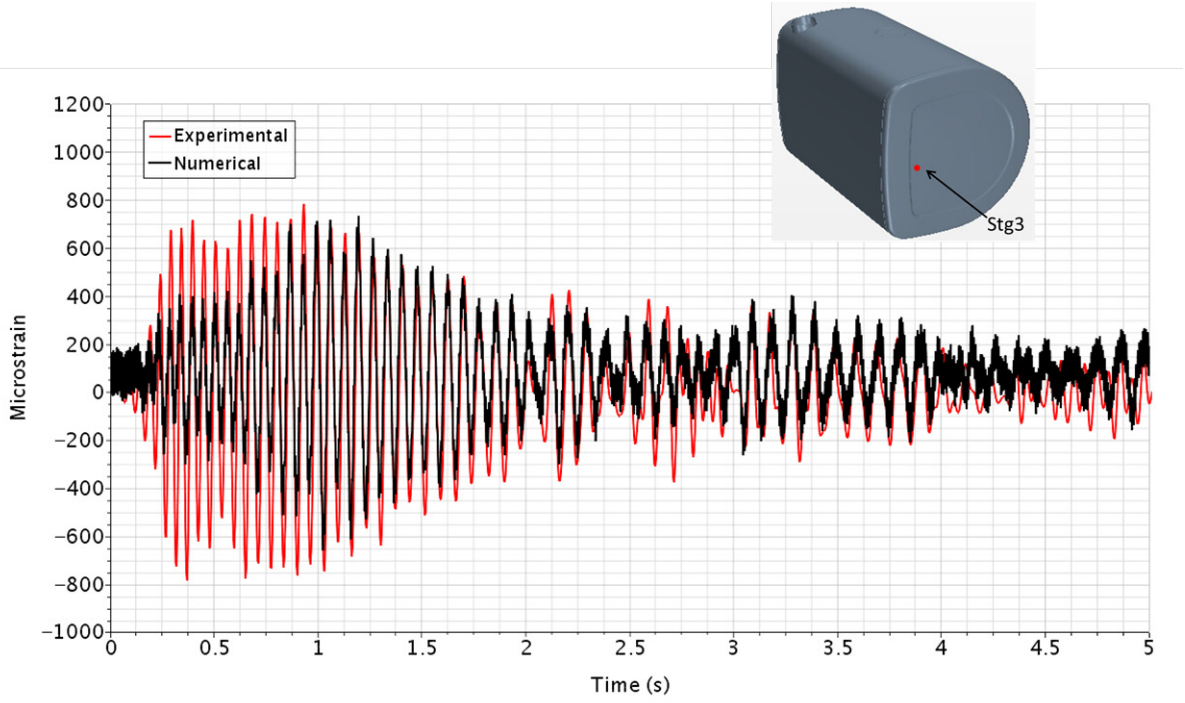

(b) 80% Filling

Figure A.5: Comparison of strains obtained from *one-way coupled* simulations and experimental results at strain gauge *Stg*3 for 60% and 80% fill levels